The Astrophysical Journal, 764:117 (16pp), 2013 February 20 doi:10.1088/0004-637X/764/2/117

THE VIRUS-P EXPLORATION OF NEARBY GALAXIES (VENGA): THE X_{CO} GRADIENT IN NGC 628

Guillermo A. Blanc[1], Andreas Schruba[2], Neal J. Evans II[3], Shardha Jogee[3], Alberto Bolatto[4], Adam K. Leroy[5], Mimi Song[3], Remco C. E. van den Bosch[6], Niv Drory[7], Maximilian Fabricius[8], David Fisher[4], Karl Gebhardt[3], Amanda Heiderman[3], Irina Marinova[3], Stuart Vogel[4], and Tim Weinzirl[3]
[1] Observatories of the Carnegie Institution for Science, Pasadena, CA, USA
[2] Astronomy Department, California Institute of Technology, Pasadena, CA, USA
[3] Astronomy Department, The University of Texas at Austin, Austin, TX, USA
[4] Department of Astronomy, University of Maryland, College Park, MD, USA
[5] National Radio Astronomy Observatory, Charlottesville, VA, USA
[6] Max Planck Institute for Astronomy, D-69117 Heidelberg, Germany
[7] Instituto de Astronomia, Universidad Nacional Autonoma de Mexico, Mexico DF, Mexico
[8] Max Planck Institute for Extraterrestrial Physics, D-85740 Garching, Germany
Received 2012 August 16; accepted 2012 December 13; published 2013 January 30

ABSTRACT

We measure the radial profile of the ^{12}CO(1–0) to H_2 conversion factor (X_{CO}) in NGC 628. The Hα emission from the VENGA integral field spectroscopy is used to map the star formation rate (SFR) surface density (Σ_{SFR}). We estimate the molecular gas surface density (Σ_{H2}) from Σ_{SFR} by inverting the molecular star formation law (SFL), and compare it to the CO intensity to measure X_{CO}. We study the impact of systematic uncertainties by changing the slope of the SFL, using different SFR tracers (Hα versus far-UV plus 24 μm), and CO maps from different telescopes (single-dish and interferometers). The observed X_{CO} profile is robust against these systematics, drops by a factor of two from $R \sim 7$ kpc to the center of the galaxy, and is well fit by a gradient $\Delta\log(X_{CO}) = 0.06 \pm 0.02$ dex kpc^{-1}. We study how changes in X_{CO} follow changes in metallicity, gas density, and ionization parameter. Theoretical models show that the gradient in X_{CO} can be explained by a combination of decreasing metallicity, and decreasing Σ_{H2} with radius. Photoelectric heating from the local UV radiation field appears to contribute to the decrease of X_{CO} in higher density regions. Our results show that galactic environment plays an important role at setting the physical conditions in star-forming regions, in particular the chemistry of carbon in molecular complexes, and the radiative transfer of CO emission. We caution against adopting a single X_{CO} value when large changes in gas surface density or metallicity are present.

Key words: galaxies: abundances – galaxies: ISM – galaxies: spiral – ISM: clouds – ISM: molecules

Online-only material: color figures

1. INTRODUCTION

Measuring and studying molecular gas in galaxies is fundamental to understanding star formation, and the physical processes setting the balance between the different phases of the interstellar medium (ISM). Molecular hydrogen (H_2) accounts for the bulk of the mass in molecules in the universe, but its observable transitions are rarely excited at the typically cold temperatures ($\sim$10 K) of the gas inside giant molecular clouds (GMCs). To overcome this observational difficulty, the second most abundant molecule in GMCs, the carbon monoxide molecule $^{12}C^{16}O$ (hereafter CO), is typically used as a proxy for estimating the total mass in H_2. Rotational CO transitions, observed at millimeter (mm) wavelengths, can be easily excited under the typical density and temperature conditions in GMCs, and are therefore bright enough to be detectable in single molecular clouds in the Milky Way (MW), galaxies within the Local Group, across the disks of nearby galaxies out to distances of $\sim$10 Mpc, and even out to high redshifts by integrating the emission over whole galaxies.

Using CO emission to estimate the H_2 mass requires either knowledge of the CO intensity to H_2 column density conversion factor,

$$X_{CO} = \frac{N(H_2)}{I(CO)}, \quad (1)$$

which for Galactic molecular clouds in the vicinity of the Sun has typical values of 2–4 $\times 10^{20}$ cm^{-2} (K km s^{-1})$^{-1}$ (Kennicutt & Evans 2012, and references therein), or, alternatively, the CO luminosity to total mass conversion factor $\alpha_{CO} = M_{H2}/L(CO)$, which unlike X_{CO} includes a factor of 1.36 for the contribution of helium to the total mass.[9]

Constraining the appropriate value of this conversion factor and establishing how it changes under the different physical conditions present across different environments inside and across galaxies is of paramount importance if astrophysical interpretations regarding the molecular ISM are to be drawn from CO data. Of particular interest is the metallicity dependence of X_{CO}, as deep observations with current facilities, and the advent of new and more powerful telescopes like ALMA and CCAT, allow the detection of CO in dwarf galaxies, the outskirts of the disks of massive spirals, and high-redshift systems, where the heavy element abundance is expected to be low.

A series of studies have used different techniques to explore the possibility of a changing X_{CO} across different types of galaxies in the nearby universe. These include virial mass measurements of individual GMCs in the MW, the Local Group, and nearby spirals (e.g., Wilson 1995; Blitz et al. 2007; Bolatto et al. 2008; Fukui & Kawamura 2010, and references therein); estimating the molecular gas mass from dust far-IR emission modeling while constraining the dust-to-gas ratio and the contribution from atomic hydrogen (Israel 1997; Leroy et al. 2011, 2012); and using the star formation rate (SFR) under the assumption of a known molecular gas depletion timescale to

[9] We report our results in terms of X_{CO}, but α_{CO} can be easily derived using the following relation: α_{CO} ($M_\odot$ pc^{-2} (K km s^{-1})$^{-1}$) = X_{CO} (cm^{-2}(K km s^{-1})$^{-1}$)/(4.6 $\times 10^{19}$).

estimate the amount of H_2 (Schruba et al. 2012; McQuinn et al. 2012). A consistent picture seems to arise from these studies, in which X_{CO} shows higher values for lower metallicity systems. The difference can be dramatic for the lowest metallicity dwarfs in the local universe, where the conversion factor can be 10–100 times higher than in the MW. This increase is most likely driven not only by a decrease in the carbon and oxygen abundances, but mainly by a drop in the optical depth within GMCs due to a lower abundance of dust. The latter translates in the CO/C^+ dissociation boundary moving inward within these clouds, leaving behind large envelopes of "CO dark" molecular gas (e.g., Bolatto et al. 1999).

On the other hand, studies of molecular gas in merging and starburst galaxies (typically ultra-luminous infrared galaxies, ULIRGS) based on virial mass measurements, dust emission modeling, and column density estimation from optically thin transitions of CO isotopes, find X_{CO} values which are factors of a few lower than the typical MW values in the solar vicinity (Wild et al. 1992; Shier et al. 1994; Mauersberger et al. 1996; Solomon et al. 1997; Downes & Solomon 1998; Bryant & Scoville 1999; Meier et al. 2010). The same effect is observed for ULIRGS and submillimeter galaxies (SMGs) at high redshift ($z > 1$) by Solomon & Vanden Bout (2005) and Tacconi et al. (2008). This effect is thought to be caused by the impact of higher gas temperatures and stronger turbulence on the brightness temperature of the CO line and the escape probability of CO (1–0) photons. Since the CO(1–0) transition is typically optically thick, the broadening of the line width (Δv) induced by higher levels of turbulence in these high-density environments promotes the escape of CO(1–0) photons (Shetty et al. 2011). Interestingly, the X_{CO} dependence with metallicity mentioned in the last paragraph has also been observed in a sample of more "normal" star-forming galaxies at high redshift by Genzel et al. (2012) using a method similar to the one used in this work.

These observational efforts to measure changes in X_{CO} across different environments have been accompanied in the last few years by detailed theoretical modeling attempts to understand how CO radiative transfer depends on the physical conditions of the ISM. A series of studies using analytic models, numerical simulations, and combinations of both, have examined the dependence of X_{CO} with metallicity, gas temperature, gas dynamics, and the local radiation field (e.g., Krumholz et al. 2011; Shetty et al. 2011; Narayanan et al. 2012; Feldmann et al. 2012a), although see early work by Dickman et al. (1986) and Maloney & Black (1988).

Considering the fact that X_{CO} changes from galaxy to galaxy depending on the average physical conditions of the ISM, it would not be surprising if it also changes within galaxies, depending on the local physical conditions present in different environments inside an individual system. For years, this has been known to be the case in our own Galaxy. The value of X_{CO} has been shown to change as a function of galactocentric radius in the MW using a series of different techniques: dust emission modeling (Sodroski et al. 1995), measurements of gamma-ray emissivity from cosmic-ray gas interactions (Digel et al. 1996; Strong et al. 2004; Abdo et al. 2010), and direct virial mass measurements of GMCs (Arimoto et al. 1996; Oka et al. 1998). All these studies find a decrease in X_{CO} from the typical values measured near the solar radius ($2–4 \times 10^{20}$ cm^{-2} (K km s^{-1})$^{-1}$) toward smaller galactocentric radii, with the conversion factor reaching typical starburst/merger type values of $0.1–0.5 \times 10^{20}$ cm^{-2} (K km s^{-1})$^{-1}$ in the Galactic center. It is not clear from current studies if the X_{CO} radial profile in the MW follows a smooth gradient or if it is fairly constant across the Galactic disk and falls sharply at some intermediate radius.

Measurements of the spatial distribution of X_{CO} within spiral galaxies are scarce in the literature, and the subject remains highly unexplored from an observational perspective. Observations of the optically thin CO isotopes ^{13}CO and $C^{18}O$, and dust continuum emission, have been used to show that X_{CO} is a factor of 2–4 lower than the typical solar vicinity MW values in the central regions of the nearby barred spirals NGC 6946 and Maffei 2 (Meier & Turner 2004; Meier et al. 2008), confirming the results from an earlier study of NGC 253, IC 342, Maffei 2, and NGC 6946 by Wall et al. (1993). Similar work by Vila-Vilaró (2008) has shown a decreased X_{CO} factor in the central kiloparsec of NGC 5194 (a.k.a. M51a). Using an independent method based on estimating the dust mass distribution by conducting radiative transfer modeling of optical and near-IR images of galaxies, and assuming a constant dust-to-gas ratio, Regan (2000) also finds low X_{CO} values in the central regions (<1.5 kpc) of NGC 1068, NGC 1530, NGC 2903, and NGC 6946. These results are consistent with what is observed in the MW. The radial profile of X_{CO} out to large radii in spiral galaxies other than the MW remains largely unexplored.

Only three published measurements of the X_{CO} radial profile for spiral galaxies other than the MW are known to the authors. First is the work of Arimoto et al. (1996) on NGC 5194 (M51a), who use GMC virial mass estimates to find that X_{CO} follows a linear gradient inside one effective radius in this galaxy. Their measurements are based on the data of Adler et al. (1992) which has a ~350 pc beam size, and we do not consider virial masses measured on such physical scales to be reliable. Second is the high-resolution (beam size ~20 pc) study of GMCs in M33 by Rosolowsky et al. (2003), who use virial masses derived from CO line widths to find a flat X_{CO} distribution across the galaxy, even in the presence of a 0.8 dex change in metallicity across their sample. And, finally, the recently published dust modeling study of a large sample of nearby spirals by Sandstrom et al. (2012), which is discussed in Section 4 (see also Aniano et al. 2012). The spatial distribution of the conversion factor in external galaxies is the subject of this paper, in which we study the radial profile of the X_{CO} across the disk of the nearby face-on Sc galaxy NGC 628.

Our method to measure X_{CO} is based on the correlation observed over many orders of magnitude between the SFR surface density and the surface density of molecular gas in the ISM of star-forming galaxies. This relation, typically known as the "star formation law" (SFL) or the "Schimdt–Kennicutt law" (Schmidt 1959; Kennicutt 1998), has been recently constrained in a spatially resolved manner across the disks of nearby spiral galaxies (Kennicutt et al. 2007; Bigiel et al. 2008; Blanc et al. 2009; Verley et al. 2010; Onodera et al. 2010; Schruba et al. 2011; Liu et al. 2011; Rahman et al. 2012). Although debate persists regarding the actual value of the SFL slope, which is subject to a series of systematic uncertainties related to background subtraction, cloud sampling, and fitting methods (see discussions in Blanc et al. 2009; Rahman et al. 2012; Calzetti et al. 2012), its normalization is consistent with a depletion timescale for molecular gas of ~2 Gyr at the typical molecular gas surface densities observed across the disks of nearby spirals ($\Sigma_{H2} = 10–100\ M_\odot$ pc^{-2}; e.g., Leroy et al. 2008; Rahman et al. 2012). This relation can be used to derive the molecular gas surface density from the observed SFR surface density across the disk of a galaxy, therefore permitting the measurement of X_{CO} by comparison to CO intensity maps.

We describe the multi-wavelength data sets used in this work in Section 2, and our method for estimating X_{CO} in Section 3. We test the robustness of our method to systematic uncertainties by changing the assumed value for the slope of the molecular SFL, using different SFR indicators, and CO maps from different telescopes (both single-dish and interferometers). Our results are presented in Section 4, where we present the observed X_{CO} radial profile of NGC 628 and compare it to that derived from dust emission modeling using *Spitzer+Herschel* photometry (Sandstrom et al. 2012). In Sections 5 and 6 we discuss the possible physical origins for the observed spatial distribution in X_{CO}, including the roles of metallicity, gas surface density, and the local UV radiation field. Finally, we provide our conclusions in Section 7. For NGC 628, we assume an inclination of $i = 8.^{\circ}7$ and a distance of 8.6 Mpc (Herrmann et al. 2008).

2. DATA

2.1. VENGA Integral Field Spectroscopy

All the measurements of nebular emission lines used to estimate the metallicity, ionization parameter, dust extinction through the Balmer decrement, and the Hα SFR, are made on the Mitchell Spectrograph (formerly VIRUS-P) integral field unit (IFU) data cube of NGC 628 produced by the VENGA survey (Blanc et al. 2010). The data-cube samples a rectangular area of $5.'2 \times 1.'7$ centered in the nucleus of the galaxy, and has a spatial resolution of $5.''6$ FWHM. The spectra cover the 3555–6790 Å wavelength range with an instrumental spectral resolution of $\simeq$5 Å FWHM. At the assumed distance of NGC 628 the VENGA spatial resolution corresponds to $\sim$235 pc, a few times larger than the typical sizes of large GMCs ($\lesssim$60 pc; Heyer et al. 2001) and individual H II regions ionized by single clusters ($\lesssim$120 pc; Gutiérrez et al. 2011). The observations, data reduction, and calibrations will be described in an upcoming publication.

2.2. GALEX Far-UV and Spitzer MIPS 24 μm Data

To ensure that our results are robust against the choice of the SFR tracer used, along with the VENGA Hα derived SFRs, we use a linear combination of far-ultraviolet (FUV) and mid-infrared (mid-IR) 24 μm emission. The former traces unobscured star formation, while the latter recovers dust obscured star formation by means of reprocessed UV radiation reemitted as thermal IR emission from heated interstellar dust grains. A number of calibrations have been proposed to use linear combinations of obscured and unobscured tracers to estimate the SFR (Calzetti et al. 2007; Leroy et al. 2008, 2012; Kennicutt et al. 2009; Hao et al. 2011; Murphy et al. 2011).

We use the *Galaxy Evolution Explorer* (*GALEX*) FUV image of NGC 628 from the *GALEX* Nearby Galaxy Survey (Gil de Paz et al. 2007) which samples the 1350–1750 Å wavelength range, has a point-spread function (PSF) FWHM of $4.''5$, and is deep enough for us to measure the FUV flux at high signal-to-noise ratio over the whole area of interest. To trace the IR dust emission we use the MIPS 24 μm data of NGC 628, taken as part of the Spitzer Infrared Nearby Galaxy Survey (SINGS; Kennicutt et al. 2003) and the Local Volume Legacy survey (Dale et al. 2009). The map has a PSF FWHM of $6''$ and like the FUV map, it is deep enough for us to measure the 24 μm flux over the whole area of interest in this paper. The data processing of both the FUV and 24 μm maps, including the suppression of backgrounds and the masking of foreground stars is detailed in Leroy et al. (2012).

2.3. HERACLES, BIMA-SONG, and CARMA CO Data

We use three independent data sets to measure I(CO) across the disk of NGC 628. The Heterodyne Receiver Array CO Line Extragalactic Survey (HERACLES; Leroy et al. 2009) CO(2–1) map, obtained at the IRAM 30 m single-dish telescope, has a beam size of $13.''6$ and rms noise of $\sim$22 mK per 2.6 km s^{-1} channel, which translates into a 1σ limit on the molecular gas surface density of $\Sigma_{H_2} \sim 3\ M_{\odot}$ pc^{-2}. Following Schruba et al. (2011) we assume a constant CO(2–1)/CO(1–0) line ratio of 0.7 to estimate I(CO) from the HERACLES data.

The Berkeley–Illinois–Maryland Array (BIMA) Survey of Nearby Galaxies (BIMA-SONG; Helfer et al. 2003) CO(1–0) map combines zero spacing single-dish data from the NRAO 12 m telescope and interferometric BIMA C and D array data, resulting in a map with a robust beam size of $6.''2$, and rms noise of 51 mJy beam^{-1} in a 10 km s^{-1} channel or $\Sigma_{H_2} \sim 13\ M_{\odot}$ pc^{-2}.

Finally, the CARMA CO(1–0) map of NGC 628 (Rahman et al. 2012) has a spatial resolution of $3.''6$ and rms noise of $\sim$20 mJy beam^{-1} in a 10 km s^{-1} channel ($\Sigma_{H_2} \sim 5 M_{\odot}$ pc^{-2}). We convolve the BIMA-SONG and CARMA maps with a Gaussian kernel to match the $13.''6$ PSF of the HERACLES map, which corresponds to $\sim$570 pc at the assumed distance to NGC 0628. The three PSF-matched CO maps are shown in Figure 1.

In order to account for systematic errors in the absolute flux calibration of the data cubes, and in the assumed CO(2–1) to CO(1–0) conversion factor, we scale the maps to match the total CO(1–0) luminosity of the HERACLES map in the inner 5 kpc of the galaxy. We find scaling factors of 1.36 and 1.36 for the BIMA-SONG and CARMA maps, respectively. Figure 2 presents both the scaled and original flux measurements in each of the radial bins over which we will measure X_{CO} (see Section 3.2) for the three maps. The $\sim$30% difference implied by these scaling factors is consistent with the systematic uncertainties in the absolute flux calibration of the three data sets, and the observed scatter in the CO(2–1) to CO(1–0) ratio across the HERACLES galaxies (Leroy et al. 2009). Assuming that the CO(2–1) to CO(1–0) ratio has no significant radial dependence, these corrections only introduce a scaling in the derived X_{CO} factors. Since we are interested in measuring relative changes in X_{CO} within the galaxy, a scaling of this type does not affect our results.

The radial dependence in the CO(2–1) to CO(1–0) ratio across the disk of spiral galaxies has been studied by Leroy et al. (2009) by comparing the CO(2–1) emission in the HERACLES maps to the Nobeyama 45 m single-dish CO(1–0) maps of (Kuno et al. 2007; see Figure 34 in Leroy et al. 2009). Although the scatter seen in the line ratio is large, no evidence for a radial dependence is seen outside the very central parts of the galaxies ($R < 0.05\ R_{25}$). Furthermore, as will be discussed in Section 4, the relatively good consistency between the different data sets (see also Figure 2), and the agreement between our measured X_{CO} radial profiles and independent measurements based on dust modeling indicate that any potential radial trend in the CO(2–1) to CO(1–0) ratio is at a significantly smaller level than the radial trends seen in X_{CO}.

The consistency between the different measurements shown in Figure 2 is reassuring. While the BIMA-SONG map includes both BIMA interferometric data and NOAO 12 m single-dish data, the CARMA map is constructed without the addition of zero spacing information, and therefore lacks sensitivity on large scales. The agreement seen in Figure 2 implies that even in the outermost radial bin for which we can measure the flux in the CARMA map, the lost large-scale extended

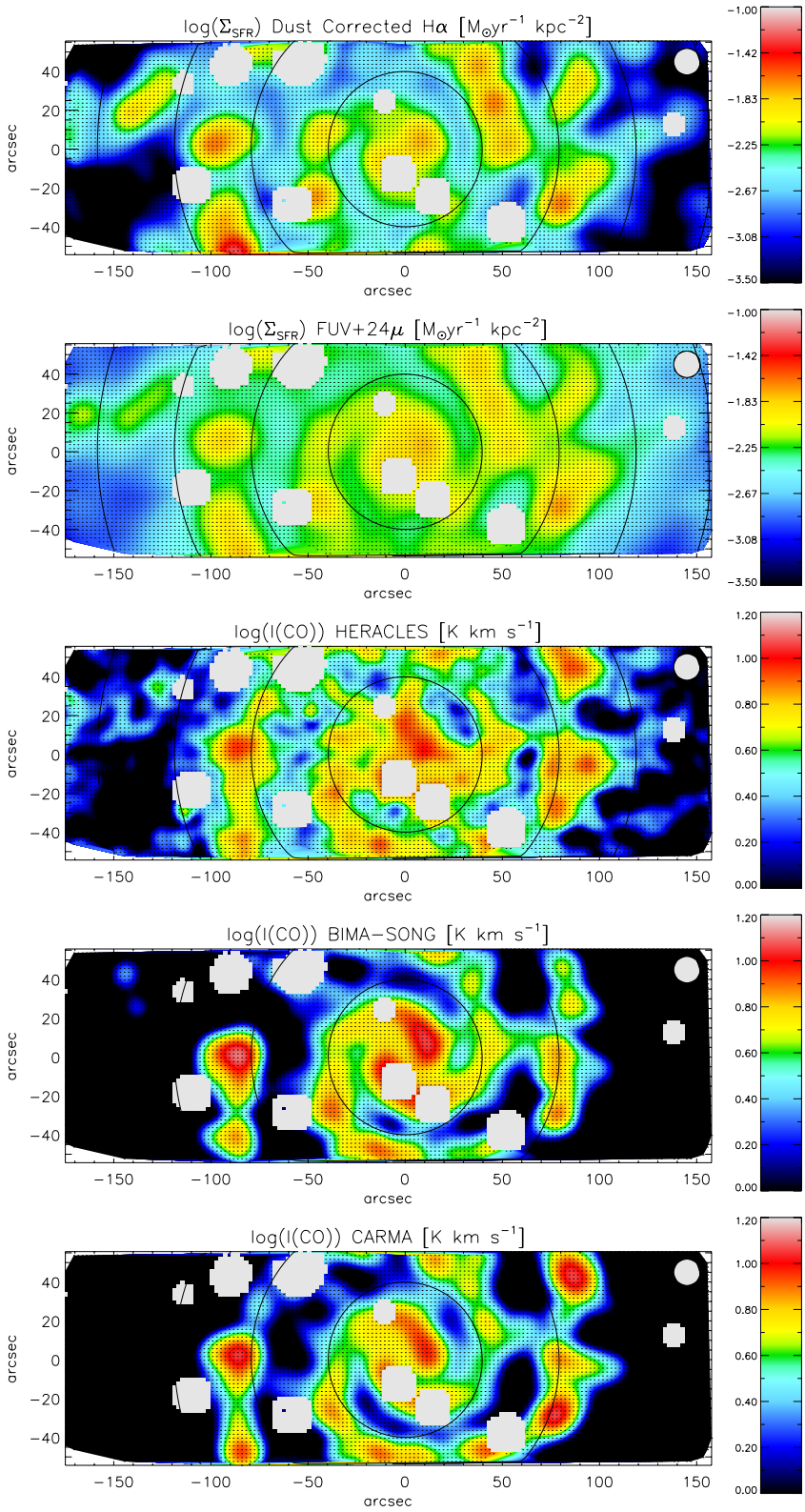

Figure 1. Maps of the Hα from VENGA and FUV+24 μm from *GALEX* and *Spitzer*-IRAC SFR surface density (top two), and the CO intensity from the HERACLES, BIMA-SONG, and CARMA data, respectively (bottom three). All maps are convolved to the HERACLES beam size of 13.″6 or 570 pc at the distance of NGC 628 (shown as a white circle in the top right corner of each map). Solid lines show the edges of the radial annuli in which we measure $X_{\rm CO}$. Gaps in the maps correspond to regions contaminated by foreground MW stars.

(A color version of this figure is available in the online journal.)

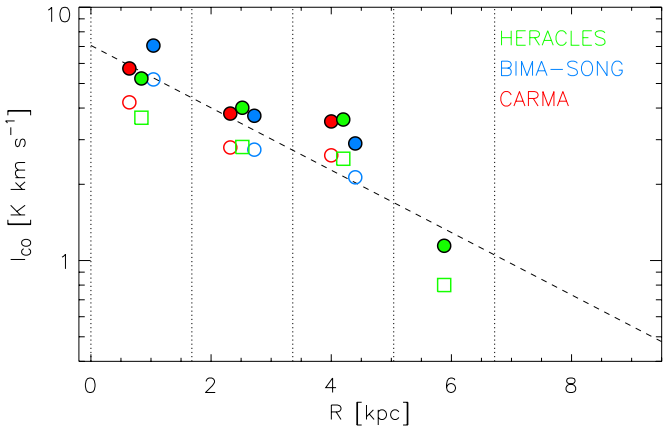

Figure 2. CO intensity as a function of radius for the four radial bins adopted in this work. Filled circles correspond to the CO(1–0) intensities after applying the scalings described in Section 2.3. Open circles show the raw BIMA-SONG and CARMA measurements before scaling them to match the HERACLES absolute flux level. Open squares show the raw CO(2–1) intensity in the HERACLES map before correcting for the assumed CO(2–1) to CO(1–0) ratio of 0.7. Data points within each radial bin have been shifted in the horizontal direction for clarity. Vertical dotted lines mark the edges of each radial bin. The error bars for each measurement, calculated as the rms per beam in each map divided by the square root of the ratio between the area of each radial bin to the beam size, are smaller than the data points themselves, and not shown. Differences in the profiles are dominated by systematic uncertainties at the 20% level.

(A color version of this figure is available in the online journal.)

emission does not contribute significantly to the total CO surface brightness.

3. ESTIMATING X_{CO}

Estimating X_{CO} (Equation (1)) requires an independent measurement of the molecular gas column density, or equivalently its surface density (Σ_{H2}), and the CO(1–0) line intensity (I(CO)). The latter is directly measured from the CO maps described in Section 2.3. We estimate Σ_{H2} from the SFR surface density (Σ_{SFR}) by inverting the molecular gas SFL (Kennicutt 1998; Kennicutt et al. 2007; Bigiel et al. 2008), which we parameterize as

$$\frac{\Sigma_{SFR}}{1\ M_\odot\ \mathrm{yr}^{-1}\ \mathrm{kpc}^{-2}} = A\left(\frac{\Sigma_{H2}}{10\ M_\odot\ \mathrm{pc}^{-2}}\right)^N. \quad (2)$$

This is a more general approach than assuming a constant molecular gas depletion timescale (Schruba et al. 2012; Genzel et al. 2012; McQuinn et al. 2012), which is equivalent to the above method for the particular case of $N = 1$.

For simplicity, we fix the SFL normalization to $A = -2.3$, which is equivalent to a molecular gas depletion timescale of 2 Gyr at $\Sigma_{H2} = 10 M_\odot$ pc^{-2}. This value is in good agreement with observations of solar metallicity spiral galaxies in the local universe (e.g., Bigiel et al. 2008; Leroy et al. 2008; Blanc et al. 2009; Schruba et al. 2011), and modifying it introduces a simple scaling in the derived X_{CO} values. We report the X_{CO} radial profile for two assumed values for the SFL slope of $N = 1.0$ and $N = 1.5$, which span the range of plausible slopes allowed by random and systematic uncertainties in current measurements of the molecular gas SFL (Calzetti et al. 2012; Kennicutt & Evans 2012, and references within).

It is important to explicitly state the assumptions underlying our method to measure X_{CO}. Mainly, we are assuming the existence of a fundamental power-law-like correlation between Σ_{H2} and Σ_{SFR}, which holds for averaged measurements of these two quantities over kiloparsec scales. The existence of such correlation across the disks of spiral galaxies has been well established by previous studies (Kennicutt et al. 2007; Bigiel et al. 2008; Blanc et al. 2009; Verley et al. 2010; Onodera et al. 2010; Liu et al. 2011; Rahman et al. 2012).

A potential caveat arises from the fact that the observed SFL in all the above-mentioned studies has been measured by assuming a constant X_{CO} factor to transform CO surface brightness into Σ_{H2}. We do not consider this to be an important limitation, as reasonable changes in X_{CO} (i.e., of the magnitude expected from theoretical models for the range of ISM physical properties present in galaxies) are not large enough to break the observed correlation between Σ_{H2} and Σ_{SFR}. On the contrary, a recent study by Narayanan et al. (2012) shows that using a changing X_{CO}, which depends on the metallicity and surface density of the molecular gas, translates into a smaller scatter around the best-fit power-law SFL for integrated measurements of galaxies, than when a single or a bimodal X_{CO} is used. Therefore, a power-law-like SFL on kiloparsec scales appears to exist independently of the assumption of a constant or changing X_{CO} factor.

A second assumption made when applying our method is that the adopted SFL does not change across the disk of the galaxy. In the linear SFL scenario (i.e., when assuming $N = 1$) this is equivalent to assuming a constant depletion timescale across the disk of the galaxy. In the linear case, our method cannot break the degeneracy between the measured values for X_{CO} and the assumed gas depletion timescale. As mentioned above, the absolute adopted value only introduces a simple scaling of X_{CO}, which is not important given that we are interested in studying relative changes across the disk of the galaxy. However, any observed changes in X_{CO} within the galaxy could, in principle, be attributed instead to changes in the depletion timescale, or equivalently, in the star formation efficiency (SFE, defined here as the inverse of the depletion time). In Section 4.3 we discuss this possibility, only to conclude that it is very unlikely that changes in the depletion time can explain the observed X_{CO} radial profile, and that the observed change in the conversion factor is most likely real. In the nonlinear case ($N = 1.5$), the depletion timescale, or equivalently the SFE, does change as a function of the local surface density of molecular gas.

3.1. Measurement of the SFR

We produce maps of Σ_{SFR} using two independent SFR indicators. First we use the Hα emission line flux, corrected for dust extinction using the Balmer decrement. The methods used to measure dust-corrected Hα fluxes and to correct the emission line map for the contribution from diffuse ionized gas are analog to the ones described in Blanc et al. (2009). An updated description of the methods used, including slight differences in the methodology used for flux calibration and construction of the IFU data cubes will be described in an upcoming publication. We use the Hα SFR calibration of Murphy et al. (2011) and Hao et al. (2011), taken from the compilation in Kennicutt & Evans (2012), which assumes a Kroupa & Weidner (2003) initial mass function (IMF). Note that this differs from the Salpeter (1955) IMF used in Blanc et al. (2009).

The second SFR indicator used is a linear combination of FUV and 24 μm flux. We use the calibration of Leroy et al. (2012), which assumes a Chabrier (2003) IMF. Calibrations based on the Kroupa and Chabrier IMFs yield nearly identical SFRs (Chomiuk & Povich 2011), which are typically $\sim$30% lower than those obtained assuming a Salpeter IMF. Since Hα and FUV photons trace star formation over different timescales (roughly 10 and 100 Myr, respectively), systematic differences

Table 1
NGC 628 X_{CO} Radial Profile

R_{bin}	N	X_{CO}-Hα[a]			X_{CO}-FUV+24 μm[a]			$\langle X_{CO}\rangle$[a]
		HERACLES	BIMA	CARMA	HERACLES	BIMA	CARMA	
0.84	1.0	1.4 ± 0.5	1.0 ± 0.4	1.3 ± 0.5	1.6 ± 0.6	1.2 ± 0.4	1.5 ± 0.5	1.3 ± 0.5
2.52		1.7 ± 0.6	1.9 ± 0.7	1.8 ± 0.6	1.7 ± 0.6	1.9 ± 0.7	1.8 ± 0.6	1.8 ± 0.6
4.20		2.1 ± 0.8	2.6 ± 0.9	2.1 ± 0.8	1.9 ± 0.7	2.4 ± 0.8	1.9 ± 0.7	2.2 ± 0.8
5.88		1.7 ± 0.8	...	...	2.5 ± 1.0	...	...	2.1 ± 0.9
0.84	1.5	1.3 ± 0.5	1.0 ± 0.4	1.2 ± 0.4	1.4 ± 0.5	1.0 ± 0.4	1.3 ± 0.5	1.2 ± 0.4
2.52		1.7 ± 0.6	1.8 ± 0.6	1.8 ± 0.6	1.6 ± 0.6	1.7 ± 0.6	1.7 ± 0.6	1.7 ± 0.6
4.20		2.0 ± 0.7	2.5 ± 0.9	2.0 ± 0.7	1.7 ± 0.6	2.2 ± 0.8	1.8 ± 0.6	2.0 ± 0.8
5.88		2.6 ± 1.0	...	...	3.0 ± 1.1	...	...	2.8 ± 1.0

Note. [a] In units of 10^{20} cm^{-2} (K km s^{-1})$^{-1}$.

between the two independent estimates might arise as a consequence of differences in star formation history. Analogously to what was done with the CO maps, we attempt to remove any systematic differences in the flux calibration of the different data sets and the SFR calibrations used by matching the total SFR within the central 5 kpc of the galaxy. This translates to us multiplying the $\Sigma_{SFR,FUV+24\,\mu m}$ map by a factor of 0.8 to match the $\Sigma_{SFR,H\alpha}$ map. Again, this correction does not affect the relative differences in X_{CO} which we are trying to measure, but only introduces a scaling of the derived values across the whole galaxy. Both maps are convolved with a Gaussian kernel in order to match the common 13.″6 FWHM PSF, and are presented in Figure 1.

3.2. Calculation of X_{CO}

We use the PSF-matched SFR maps to measure $\Sigma_{SFR,FUV+24\,\mu m}$, $\Sigma_{SFR,H\alpha}$, and I(CO) in elliptical annuli of constant galactocentric radius. We chose an annuli width of 40″ which roughly corresponds to three times the spatial FWHM of the maps, and a physical scale of 1.68 kpc at the adopted distance to NGC 628 (see Figure 1). The sensitivity of the BIMA-SONG and CARMA maps only allows the measurement of I(CO) out to 5 kpc (∼120″) which corresponds to the inner three annuli, while the HERACLES map is able to provide a reliable measurement in a fourth bin, out to a galactocentric distance of 7 kpc (∼170″). While Schruba et al. (2011) was able to measure CO emission using the HERACLES map of NGC 628 out to larger radii (∼10 kpc) using a stacking technique, here we are also limited by the coverage of the VENGA IFU observations which only reach out to ∼7.5 kpc. We use the extended stacking measurements of Schruba et al. (2011) separately in the next section to extend our measurements to larger radii. Having measured these three quantities ($\Sigma_{SFR,FUV+24\,\mu m}$, $\Sigma_{SFR,H\alpha}$, and I(CO)), we use Equation (2) to obtain Σ_{H2}, and we transform it to units of column density. Finally we calculate X_{CO} for each radial bin by applying Equation (1). The central radius and measured X_{CO} values for each annuli are reported in Table 1.

The uncertainty in the measured X_{CO} values is dominated by the intrinsic scatter in the molecular SFL. A series of studies have shown that this quantity depends on the physical scales over which the observed surface densities are integrated (Verley et al. 2010; Onodera et al. 2010; Schruba et al. 2011; Liu et al. 2011). For the large physical scales considered in this work (∼4 kpc given the mean area of our radial bins), we assume a value of ∼0.15 dex for the scatter, which we propagate into the uncertainty in X_{CO}. Thanks to the high signal-to-noise ratio of the data sets and the large areas over which we are integrating, the contribution from random errors in Σ_{SFR}, which includes photometric errors in the $H\alpha$ and $H\beta$ (the latter entering in the Balmer decrement dust extinction correction), and in the FUV and 24 μm fluxes, as well as from noise in the CO maps, is negligible (a factor of ∼5 smaller) compared to the scatter in the molecular SFL.

4. THE X_{CO} RADIAL PROFILE

4.1. Consistency between Different Data Sets

In Figure 3 we present the measured X_{CO} factor as a function of galactocentric radius for the six combinations of data sets (two SFR indicators and three CO maps from different telescopes), and two different assumptions for the molecular SFL slope ($N = 1.0$ and 1.5). At all radii, all combinations of data sets are consistent with each other within the 1σ formal error bars, and show the same systematic trend of increasing X_{CO} with radius. This implies that our results are robust against potential systematics associated with the adopted SFR indicator, and the nature of the CO maps utilized (single-dish versus interferometer, CO(1–0) versus CO(2–1)). The consistency between different data sets also confirms that photometric errors are not a significant source of uncertainty, when compared to the systematic errors associated with the scatter in the SFL.

As can be seen in Figure 1, the agreement between the Hα and FUV+24 μm SFR maps is good. After performing the scaling described in Section 3.1, the ratio of the two different SFRs measured in the inner four radial bins shows an rms scatter of 13%. When analyzing the morphology of these two SFR tracers we note a strong similarity. All individual star-forming regions picked up by one method are also recovered by the other. This is important as it implies that the dust-corrected Hα method is not missing a significant fraction of completely obscured star formation which should be recovered by dust emission at 24 μm.

While both maps trace the same structures, a more detailed inspection shows that the FUV+24 μm SFR map does seems to have a more diffuse morphology than the Hα SFR map. In particular more diffuse FUV+24 μm emission is seen in the inter-arm regions of the galaxy, while the Hα emission seems to be more concentrated in the arms. This is consistent with the typical star formation timescales traced by these two methods. Hα traces young stars ($\leqslant$10 Myr), which are seen close to their birthplaces, while both FUV and 24 μm emission receive a significant contribution from older stars ($\leqslant$100 Myr) which are more homogeneously distributed across the galactic disk, and not necessarily associated with the spiral arms.

The morphological agreement between the different CO maps is also very good. After applying the scalings described in Section 2.3 the CO luminosities in the inner three radial bins

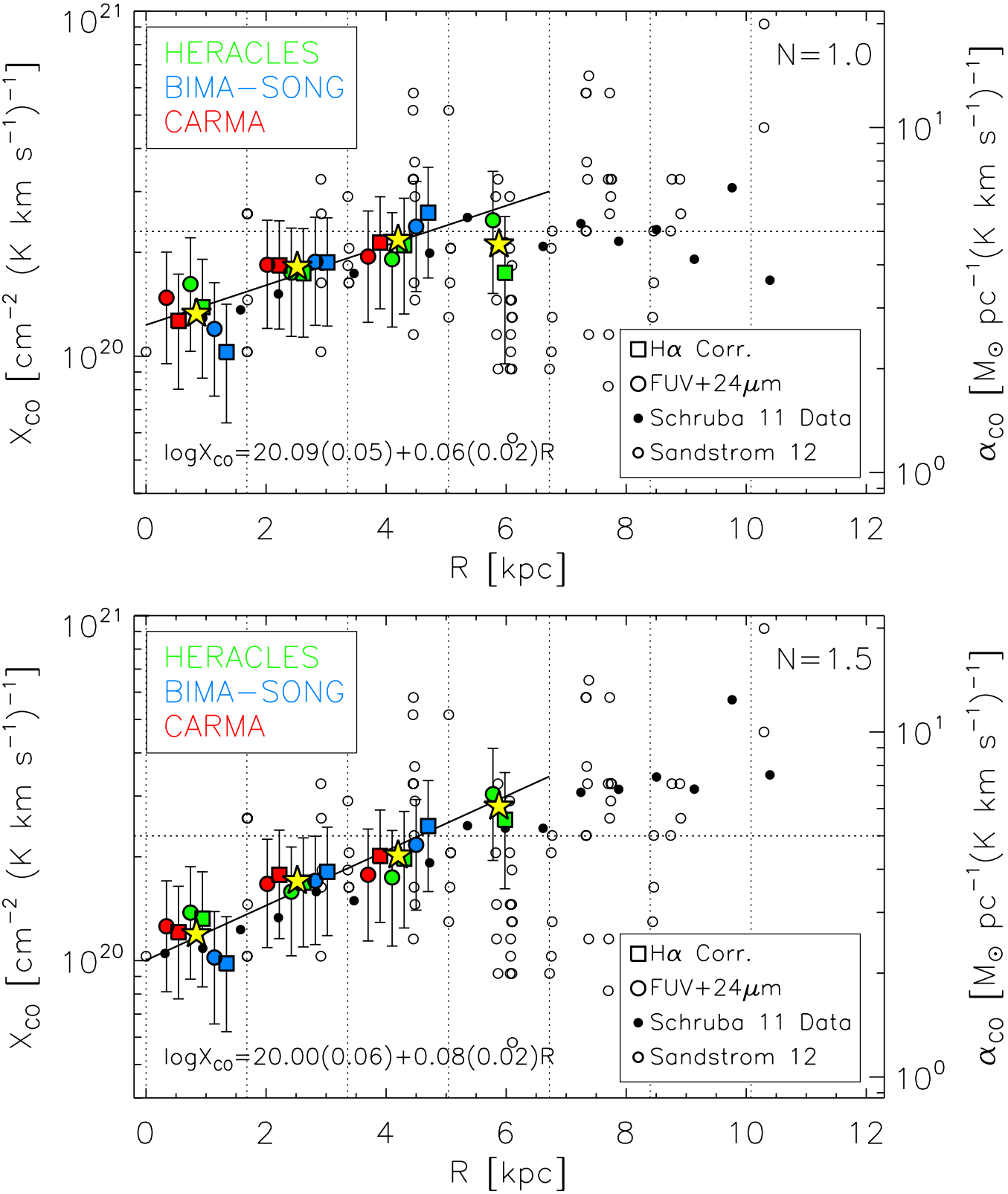

Figure 3. Radial profile of X_{CO} in NGC 628. The top and bottom panels present results for an SFL slope of $N = 1.0$ and $N = 1.5$, respectively. Measurements using the HERACLES, BIMA-SONG, and CARMA maps are shown in green, blue, and red, respectively. Measurements based on Hα and FUV+24 μm SFRs are shown as large color squares and circles, respectively. Data points within each radial bin have been shifted in the horizontal direction for clarity. Yellow stars show the average of these measurements in each radial bin. Vertical dotted lines mark the edges of each radial bin, and the horizontal dotted line marks the MW X_{CO} factor of Pineda et al. (2010). Also shown are measurements from *Spitzer+Herschel* dust SED modeling (Sandstrom et al. 2012; small open circles), and the results of applying our method to the stacked data in Schruba et al. (2011; small filled circles).

(A color version of this figure is available in the online journal.)

show a typical rms scatter of 20% (see Figure 2). The agreement justifies our adoption of a single CO (2–1)/(1–0) line ratio across the galaxy. It is interesting to note that while both the CO emission and the SFR trace similar morphological structures across the galaxy, that is, mainly the grand design spiral arms of NGC 628, a detailed comparison shows that there is not a one-to-one correlation between individual CO bright regions and regions which are bright in Hα or FUV+24 μm. This reflects the temporal dependence of the star formation process, in which recently formed star clusters disrupt and dissociate their molecular gas birth clouds by injecting both radiative and mechanical energy into their surrounding ISM. As this process takes place, an individual star-forming region evolves from a CO bright molecular complex into a 24 μm bright, highly obscured, star-forming region, which eventually dissociates and removes the bulk of the molecular gas and dust surrounding it, becoming an Hα and FUV bright region in the process. This temporal evolution translates into a spatial offset between SFR and molecular gas tracers, and is the main cause behind the need to average over large kiloparsec scales in order to do a measurement like the one presented in this work (Schruba et al. 2010; Madore 2010; Feldmann et al. 2012b; Kennicutt & Evans 2012).

In order to quantify the previous statements regarding the robustness of our measurement, we calculate the standard deviation of all $X_{\rm CO}$ measurements in each radial bin, and find it to range from a few percent to ~25% of the measured values in the worst case (outermost bin). The mean rms across all four bins corresponds to ~15% of the measured values. This dispersion is caused by a combination of different factors including systematic errors in the adopted CO(2–1)/CO(1–0) ratio, a possible systematic lack of sensitivity to low surface brightness emission in the interferometric CO maps, and potential variations in the ratio between the Hα and FUV+24 μm SFRs which might arise as the consequence of changes in the stellar populations and the properties of dust across the disk of the galaxy. The magnitude of these systematic deviations is smaller than the formal 0.15 dex (~35%) uncertainty adopted. Nevertheless, we add this dispersion in quadrature to our formal errors in order to take into account the effects of theses systematics in our error budget.

4.2. Dependence of X_{CO} on the Assumed SFL Slope

The dotted horizontal line in Figure 3 marks the canonical MW $X_{\rm CO}$ factor of 2.3×10^{20} cm^{-2} (K km s^{-1})$^{-1}$ from Pineda et al. (2010), which is adopted as the preferred value in Kennicutt & Evans (2012). While at radii >2 kpc the $X_{\rm CO}$ factor in NGC 628 is consistent with the MW value, there is an evident drop in the central 2 kpc of the galaxy, where the measured $X_{\rm CO}$ is a factor of two lower than the MW value.

The drop in the radial profile of $X_{\rm CO}$ toward the central regions is observed independently of the assumed SFL slope. A nonlinear SFL with $N > 1$ implies lower H_2 surface densities, and therefore lower derived $X_{\rm CO}$ values for high SFR surface density regions than a linear relation. Since the SFR in NGC 628, and in most disk galaxies, decreases with radius, a nonlinear slope implies an even larger drop in $X_{\rm CO}$ toward the central regions. In any case, the magnitude of the changes in $X_{\rm CO}$ between the $N = 1.0$ and 1.5 cases is smaller than the changes in $X_{\rm CO}$ observed as a function of radius across the galaxy. This implies that potential changes in the SFL slope within the galaxy would not affect our results significantly. While a sub-linear ($N < 1$) slope could reduce the magnitude of the observed drop in $X_{\rm CO}$ toward the central regions, this scenario is not currently supported by observations (Calzetti et al. 2012; Kennicutt & Evans 2012, and references within).

This dependence with the SFL slope is important, as it implies that the observed radial trend of $X_{\rm CO}$ is not a consequence of changes in the SFE with radius. Adopting a super-linear slope for the SFL is effectively testing the case in which the efficiency of star formation is enhanced in higher density regions, and as stated above, this effect only boosts the decrease of $X_{\rm CO}$ at small radii, although not significantly. We further discuss this subject in the next section.

4.3. X_{CO} Gradient and Comparison to Other Measurements

Also shown as open circles in Figure 3 are the measurements of $X_{\rm CO}$ in NGC 628 from dust spectral energy distribution (SED) modeling (Sandstrom et al. 2012). We only plot their data points with an uncertainty $\leqslant$0.4 dex in $X_{\rm CO}$. This study uses the method of Leroy et al. (2011) to simultaneously model the dust mass surface density and the dust-to-gas ratio across the disks of a sample of nearby spiral galaxies with far-IR SED measurements from the SINGS and KINGFISH (Kennicutt et al. 2011) surveys. The dust mass surface density, in combination with the dust-to-gas ratio, provides an estimate of the total gas surface density. Subtraction of the atomic component (measured from H I 21 cm maps) yields the surface density of the molecular component. This technique is completely independent of the method adopted in this work. The data points from the dust SED modeling have a typical uncertainty of 0.2 dex at $R < 7$ kpc, hence they agree with our measurements across the whole range in radii sampled by our data, and significantly show the same trend of decreasing $X_{\rm CO}$ toward the central regions of NGC 628. No scaling has been applied to the measurements in Figure 3, so the agreement is not only in the shape of the $X_{\rm CO}$ radial profile but also in its absolute value.

A similar analysis was conducted by Aniano et al. (2012) for NGC 628 and NGC 6946. While a drop in $X_{\rm CO}$ toward the center of the galaxy is evidently seen in their data for NGC 6946, the authors do not claim the detection of a changing $X_{\rm CO}$ profile in NGC 628. Inspecting their Figure 4, it is evident that the results of their measurements of $X_{\rm CO}$ in NGC 628 are subject to strong systematic uncertainties, and show large changes (from an increasing to a flat, or even decreasing, radial trend) depending on which subset of the *Spitzer*+*Herschel* data is used and the spatial resolution at which the modeling is conducted. This is not the case for NGC 6946 where different data sets at different resolutions yield consistent results. Given the large systematic uncertainties in their measurement of $X_{\rm CO}$ for NGC 628, we refrain from conducting a detailed comparison to their results.

In Section 3, we discussed the inherit degeneracy in our method between the SFL normalization constant (or equivalently the gas depletion time when $N = 1$), and the measured values of $X_{\rm CO}$. A basic assumption in this work is that of a constant SFL across the disk of NGC 628. In order to explain the data in Figure 3 solely as a variation in the normalization of the SFL would require the depletion timescale to be longer, or the SFE to be lower, by a factor of two in the central (denser) regions than in the outer disk. This is not in line with expectations from measurements of the SFE across different environments in galaxies in the local universe. A series of studies have shown that luminous infrared galaxies, ULIRGS, and SMGs, in which the molecular gas surface density is one to two orders of magnitude larger than in the disks of normal spirals, show typical

depletion timescales which are factors of 3–4 shorter than normal spiral galaxies. The difference becomes even larger (factors of 4–10 shorter) if differences in the X_{CO} factor in these systems are taken into account (Daddi et al. 2010; Genzel et al. 2010; García-Burillo et al. 2012). Although the central region (<2 kpc) of NGC 628 is only factors of a few denser than the outer disk, it would be surprising to find a reversal from the global trend seen in the SFE toward denser environments. Furthermore, the consistency between the results from this work and the independent dust SED modeling method, which is not subject to such a degeneracy between X_{CO} and the depletion timescale, is very encouraging, and gives us confidence that our working assumption is valid within the range of current uncertainties.

If we model the X_{CO} profile in the inner 7 kpc of the galaxy as a simple gradient of the form:

$$\log(X_{CO}) = \log(X_{CO,0}) + \Delta\log(X_{CO}) \times R \quad (3)$$

a fit to the average of the six measurements in each radial bin (two measurements in the outer bin), which are shown as stars in Figure 3, yields X_{CO} gradients of $\Delta\log(X_{CO}) = 0.06 \pm 0.02$ dex kpc^{-1} for $N = 1$, and $\Delta\log(X_{CO}) = 0.08 \pm 0.02$ dex kpc^{-1} for $N = 1.5$.

The best-fit central X_{CO} values are $X_{CO,0} = 1.3 \pm 0.2 \times 10^{20}$ cm^{-2} (K km s^{-1})$^{-1}$ for $N = 1$ and $X_{CO,0} = 1.1 \pm 0.2 \times 10^{20}$ cm^{-1} (K km s^{-1})$^{-1}$ for the $N = 1.5$ case. Our data imply that X_{CO} in the galactic center of NGC 628 is about a factor of two higher than the typical values of $X_{CO,0} = 0.1$–0.5×10^{20} cm^{-2} (K km s^{-1})$^{-1}$ measured in the MW Galactic center (e.g., Sodroski et al. 1995; Strong et al. 2004; Oka et al. 1998).

Inspecting Figure 3, particularly for the $N = 1$ case, it is not evident if the radial profile of X_{CO} follows a linear gradient, or if it is fairly flat across the disk of the galaxy, and only drops in the central regions. Our measurements are limited at $R > 7$ kpc by the sensitivity of the HERACLES CO map, and the coverage of the VENGA IFU data cube. The dust SED modeling data points go out to ~10 kpc, but they show a very large scatter, and at such large radii, the uncertainty in their measurements increases sharply, so it is not easy to draw conclusions from these data points regarding the behavior of X_{CO} at large radii.

In an attempt to extend our measurements into the outer disk of the galaxy, we use our method to estimate X_{CO} on the stacked CO and FUV+24 μm radial profiles of NGC 628 presented in Schruba et al. (2011). In this work, the authors use the 21 cm H I velocity field to predict the exact wavelength of the CO line at every position in the HERACLES data cube. This information is then used to register and stack the spectra of all spatial resolution elements in 15″ wide radial bins across the galaxy. Using this technique, Schruba et al. (2011) is able to significantly measure I(CO) out to ~10 kpc. They also measure the FUV+24 μm SFR profile using the same maps used in this work. We show these measurements as filled black circles in Figure 3. Error bars are not shown for clarity, but they are also dominated by the intrinsic scatter in the SFL, and are of the same order of magnitude as the error bars for the measurements in the inner regions of the galaxy (color filled circles and squares). The results of this exercise are inconclusive. While in the $N = 1$ case the value of X_{CO} seems to flatten around the canonical MW value, if we assume $N = 1.5$ X_{CO} such hints for a flattening in the outer regions are less obvious but still present.

As will be further discussed in Section 5, NGC 628 shows a metallicity gradient described by a fairly constant slope out to ~1 R_{25} (~13 kpc; Rosales-Ortega et al. 2011). If X_{CO} scales as some power of the metal abundance (Z), we would expect it to keep on increasing out to a similar radius. On the other hand there are reasons why a flattening in the radial profile might be expected. For example, if X_{CO} increases with a decreasing molecular cloud surface density, as proposed by Narayanan et al. (2012), and the GMCs in the outer disk have uniform properties but become denser toward the central regions, a certain level of flattening in the X_{CO} profile might occur, although the metallicity dependence discussed above should still be present. We will explore the role of the molecular gas surface density and the UV radiation field in Section 6, and will discuss this possibility in more detail.

For all the results presented in the following sections, we adopt the $N = 1.0$ case. We have checked that changing the slope to $N = 1.5$ does not significantly affect the rest of the results presented below.

5. RELATING THE X_{CO} AND METALLICITY GRADIENTS

As discussed in Section 1, both observations of nearby and high-redshift galaxies (Arimoto et al. 1996; Israel 1997; Bolatto et al. 2008; Leroy et al. 2011; Schruba et al. 2012; Genzel et al. 2012) as well as theoretical models (Krumholz et al. 2011; Narayanan et al. 2012; Feldmann et al. 2012a) indicate that X_{CO} is a decreasing function of metallicity. The main physical process behind this dependence is the role that dust extinction, which is directly linked with metallicity, plays in the dissociation of CO molecules. In photodissociation regions on the edges of molecular clouds, as the metallicity and with it the dust extinction decreases, the CO to C^+ transition layer moves inward, leaving behind large envelopes of "CO dark" gas where hydrogen is still in molecular form thanks to self-shielding (Maloney & Black 1988; Bolatto et al. 1999; Glover et al. 2010). This translates into higher CO to H_2 conversion factors for lower metallically environments. While at the relatively high metallicities found across the disk of NGC 628 we do not expect to see extreme cases of completely "CO dark" molecular clouds (which might be present in extreme low metallicity galaxies like I Zw 18; Schruba et al. 2012), variations in the CO brightness of the diffuse lower density (and lower extinction) envelopes of molecular clouds as a function of metallicity are possible (Feldmann et al. 2012a).

Since most disk galaxies show radial metallicity gradients, with higher metal abundances toward the central regions (Moustakas et al. 2010, and references therein), it would be natural to attempt to relate metallicity gradients with gradients in X_{CO}. In this section we study the relation between the observed radial profile of X_{CO} in NGC 628, and its metallicity distribution. We measure the metallicity gradient using strong nebular emission lines in the VENGA IFU data, and study how the relation between X_{CO} and metallicity across the disk of the galaxy compares to that seen across galaxies in the local universe, and to the predictions of theoretical models.

5.1. The Metallicity Gradient in NGC 628

The VENGA IFU data cube provides maps of many strong nebular emission lines typically used for metallicity diagnostics. As discussed in detail in Kewley & Ellison (2008) and Moustakas et al. (2010), different strong-line methods used to measure metallicity can show large discrepancies in the derived abundances. Particularly, methods calibrated against theoretical photoionization models typically yield higher metallicities than methods calibrated against samples of H II regions with

direct electron temperature measurements (a.k.a. empirically calibrated methods). Differences as large as 0.6 dex are seen between these two families of methods. On the other hand, relative differences in metallicity from one system to another do not change drastically if different methods are applied, allowing meaningful conclusions to be drawn from comparing different samples, as long as a single method is used, or measurements using different methods are properly transformed to a common metallicity scale (Kewley & Ellison 2008). In order to study the metallicity dependence of X_{CO} across NGC 628, and compare it to previous measurements in the literature, we must not only choose a reliable strong-line abundance indicator, but we must also put ours and the literature measurements on a common metallicity scale.

Our preferred metallicity calibration is the $N2O2$ method of Kewley & Dopita (2002), which estimates the oxygen abundance from the [N I]λ6584/[O II]λ3727 ratio, and is calibrated against photoionization models. We have a series of reasons to favor this calibration. Mainly, the $N2O2$ indicator is highly independent of the ionization parameter, is single valued at all metallicities, and the secondary production of nitrogen makes this indicator very sensitive to metallicity changes at high metallicities like the ones we expect in massive spiral galaxies like NGC 628 (see discussion in Kewley & Dopita 2002).

On the other hand, the metallicity compilations for the systems with measured X_{CO} values reported in Bolatto et al. (2008) and Leroy et al. (2011) are largely based on direct electron temperature measurements. The metallicities reported in Schruba et al. (2012) are on an intermediate scale, since the authors averaged the values from the two indicators used by Moustakas et al. (2010): the photoionization model calibrated R_{23} metallicities of Kobulnicky & Kewley (2004, hereafter $R_{23} - KK04$) and the empirically calibrated R_{23} method of Pilyugin & Thuan (2005, hereafter $R_{23} - PT05$).

We decide to apply a simple offset in metallicity to both our $N2O2$ measured values in NGC 628 and the reported metallicity values in Schruba et al. (2012), to put them on a common scale with the direct method metallicities reported in Bolatto et al. (2008) and Leroy et al. (2011). To do so, we measured the metallicity in the NGC 628 data cube using the three methods mentioned above ($N2O2$, $R_{23} - KK04$, and $R_{23} - PT05$), and measure the mean offset in the recovered metallicity values between different methods for all spaxels above an Hα surface brightness cut chosen to trace H II regions.[10] As expected, both the $N2O2$ and the average between the $R_{23} - KK04$ and $R_{23} - PT05$ methods (i.e., the method used in Schruba et al. 2012) yield higher metallicities than $R_{23} - PT05$ alone, which is calibrated against direct method measurements on H II regions and should fall in a similar scale to the values reported in Bolatto et al. (2008) and Leroy et al. (2011). We find and apply mean offsets of −0.66 dex and −0.35 dex to the $N2O2$ and Schruba et al. (2012) metallicities before doing any comparisons. These values are in good agreement with the 0.6 dex offset found between $R_{23} - KK04$ and $R_{23} - PT05$ by Moustakas et al. (2010).

Note that we decided to apply a single offset in metallicity instead of using the conversion relations of Kewley & Ellison (2008). This is done deliberately, as the nonlinear nature of these conversions imply that the measured metallicity gradient would change its value depending on the adopted scale. Also, these conversions have been calibrated against integrated measurements of galaxies, and it is not clear how valid it would be to apply them to spatially resolved regions within a single object. This issue will be the subject of a future publication in which we will analyze the impact of different methods on the observed metallicity distributions in the VENGA galaxies. For the purpose of this work, we prefer to conserve the shape of the gradient as measured by the $N2O2$ method which we consider more robust than other formulations. In any case, using the Kewley & Ellison (2008) conversions, or using $R_{23} - PT05$ directly on our data instead of $N2O2$ does not significantly change our results.

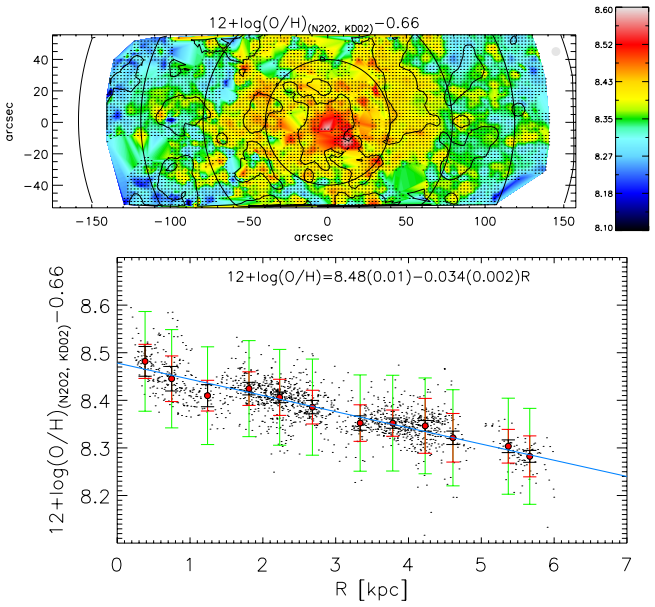

Figure 4. Spatial $N2O2$ metallicity distribution in NGC 628 measured from the VENGA data cube, offset to match the "empirical method" metallicity scale. The top panel shows a two-dimensional map of 12+log(O/H). Thick contours mark regions above the Hα surface brightness cut where the nebular emission is dominated by H II regions. The bottom panel shows the radial distribution in metallicity of all spaxels inside these regions (black dots). Red circles and error bars mark the median and standard deviation of all spaxels in 0.5 kpc radial bins. Black error bars show the median measurement error in each radial bin, and green error bars show the 0.1 dex intrinsic scatter associated with the $N2O2$ calibration.

(A color version of this figure is available in the online journal.)

Figure 4 presents the spatial distribution in metallicity of NGC 628. The top panel shows a two-dimensional map of 12+log(O/H), where thick contours mark regions above the Hα surface brightness cut where the nebular emission is dominated by H II regions. The bottom panel shows the distribution of metallicity as a function of galactocentric radius for data-cube spaxels inside these regions. Black error bars show the median measurement errors in each radial bin, red error bars mark the standard deviation for all spaxels in each bin, and green error bars show the 0.1 dex intrinsic scatter associated with the $N2O2$ calibration (Kewley & Ellison 2008). We measure a gradient of $\Delta\log(O/H) = 0.036 \pm 0.002$ dex kpc^{-1}, in good agreement with the IFU measurements of Rosales-Ortega et al. (2011).

5.2. X_{CO} versus Metallicity

In Figure 5, red stars show the X_{CO} values measured in each radial annuli in NGC 628, as a function of the metallicity at

[10] All these strong-line methods have been calibrated either empirically against direct-method metallicities of H II regions, or photoionization models with densities and ionization parameters typical of H II regions, therefore they cannot be applied to low surface brightness regions in which the nebular emission is dominated by the diffuse ionized gas.

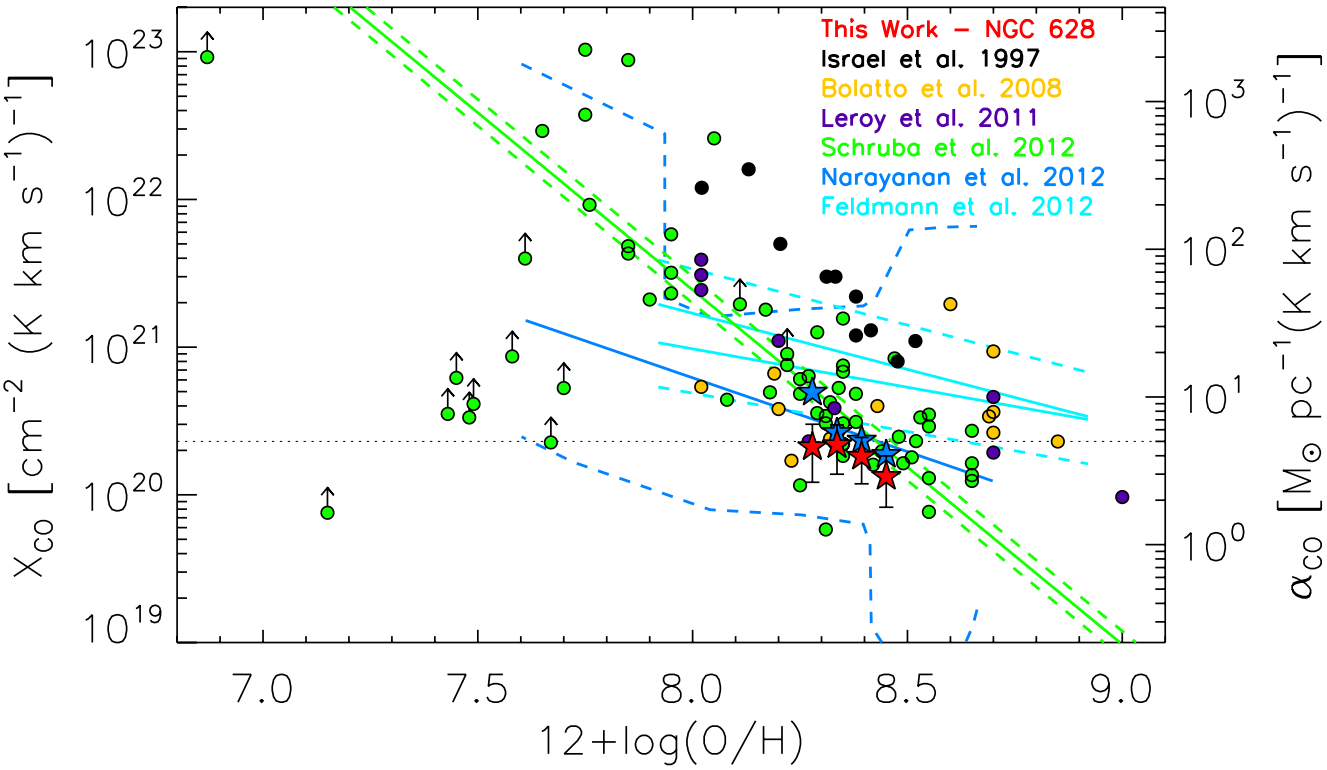

Figure 5. X_{CO} factor as a function of metallicity (12+log(O/H)). Red stars correspond to the four radial bins in NGC 628 analyzed in this work. The measurements of Bolatto et al. (2008), Leroy et al. (2011), and Schruba et al. (2012) are shown as orange, purple, and green circles. The solid and dashed green lines show the best-fit relation to the clean HERACLES sample in Schruba et al. (2012). The theoretical models of Narayanan et al. (2012) and Feldmann et al. (2012a) are also shown. For the Narayanan et al. (2012) model, the solid blue line shows the expected scaling of X_{CO} with metallicity for a constant $\Sigma_{H2} = 100\,M_\odot$ pc^{-2}, and the blue dashed lines mark the scatter in X_{CO} seen across their simulated galaxies. Blue stars mark the predictions from the model taking into account the differences in gas density for each radial bin in NGC 628. For the Feldmann et al. (2012a) model the two solid cyan lines mark, from top to bottom, their "constant line width" and "virialized" models at 4 kpc resolution. Dashed lines mark factors of two above and below the two models, respectively, which the authors state bound the expected scatter in X_{CO} for their models.

(A color version of this figure is available in the online journal.)

the radius corresponding to the center of each annuli (evaluated from the metallicity gradient measured in Section 5.1). Also shown are the data of Bolatto et al. (2008), Leroy et al. (2011), and Schruba et al. (2012),[11] as well as predictions from the theoretical models of Narayanan et al. (2012) and Feldmann et al. (2012a).

Across the disk of NGC 628, X_{CO} increases toward lower metallicity regions. This is expected from the positive and negative gradients measured for X_{CO} and the oxygen abundance, respectively (Sections 4 and 5.1). This behavior is consistent with integrated measurements of galaxies in the local universe. Both Leroy et al. (2011) and Schruba et al. (2012) see an increase in X_{CO} toward low metallicities by conducting integrated measurements across galaxies using dust mass modeling in the first case, and a similar method to the one used here in the later. The X_{CO} values inferred from GMC virial masses in Bolatto et al. (2008) do not show an obvious trend with metallicity, but are consistent with other studies given the large scatter in the observed relation. Also, as discussed in the original Bolatto et al. (2008) paper, and in Schruba et al. (2012), estimates of X_{CO} using virial mass measurements from CO observations most likely miss the "CO dark" envelopes of molecular clouds in low metallicity galaxies, as they can only trace mass enclosed in the CO emitting region. This could translate in an underestimation of X_{CO} at low metallicity in the Bolatto et al. (2008) data. The same effect could explain the constancy of X_{CO} seen by Rosolowsky et al. (2003) across 45 GMCs in M33, even in the presence of a 0.8 dex change in metallicity within their sample.

The NGC 628 data points are consistent with previous observations, especially considering the large scatter seen in the X_{CO}–metallicity relation (∼0.5 dex). The limited dynamic range in metallicity that we can sample across the inner 7 kpc of a single galaxy prevents us from being able to put strong constraints in the slope of the X_{CO}–metallicity relation. Modeling this relation as a power law of the form $X_{CO} \propto Z^{\alpha}$, Schruba et al. (2012) measures a slope of $\alpha = -2.0 \pm 0.4$ for the full HERACLES sample after rejecting starburst galaxies (green solid line in Figure 5), while Israel (1997) finds a slope of $\alpha = -2.7 \pm 0.3$ in their study of dust emission in local dwarfs. A linear fit to our data points yields a slope of $\alpha = -1.1 \pm 1.6$, shallower than previous measurements but still consistent with both Israel (1997) and Schruba et al. (2012). Again, given the limited dynamic range in metallicity of our data, and the large scatter in the X_{CO}–metallicity relation, detailed comparisons are difficult.

The slope of the observed relation in NGC 628 is also in agreement with expectations from theoretical models. At fixed molecular gas surface density, the simulations in Narayanan et al. (2012) predict a linear dependence of X_{CO} with metallicity (i.e., $\alpha = -1.0$),[12] and the study by Feldmann et al.

[11] The data points of Schruba et al. (2012) have been scaled up by a factor of 1.11 to account for the difference in the assumed depletion timescale (2.0 versus 1.8 Gyr).

[12] Note that in their model this exponent changes if one assumes constant CO brightness instead of constant Σ_{H2} because of the metallicity dependence of X_{CO} (see Equations (6) and (8) in Narayanan et al. 2012).

(2012a) predicts slopes in the −0.5 to −0.8 range, depending on the treatment given to the sub-grid gas dynamics in their simulations. Regarding the normalization of the observed relation, our data show a remarkably good agreement with the Narayanan et al. (2012) model for an assumed molecular surface density of $\Sigma_{H2} = 100\,M_{\odot}$ pc^{-2}. On the other hand, the Feldmann et al. (2012a) model, in which X_{CO} is independent of the molecular gas surface density, predicts values that are a factor of ∼4 higher than our observations. In the following section we discuss the characteristics of these models in more detail, paying particular attention to the discrepancies which arise from the different treatments given to the role of the local gas surface density at setting the X_{CO} conversion factor.

6. THE ROLE OF GAS DENSITY AND THE UV RADIATION FIELD AT SETTING X_{CO}

In the previous section we explored the role of metallicity in setting the value of X_{CO}, and discussed how well observations are described by the dependence on metallicity predicted by current theoretical models of CO emission in molecular gas. Here, we explore the dependence of X_{CO} on other physical properties like the surface density of molecular gas, and the local UV radiation field, which at the same time, affect the temperature and degree of turbulence in the ISM. Informed by the predictions of theoretical models, we examine these potential trends in the NGC 628 data, and explore if other parameters, beyond the metallicity, are important at setting the observed X_{CO} radial profile.

6.1. Further Comparison to Theory: Gas Density

In the theoretical model of Feldmann et al. (2012a), X_{CO} is a strong function of the molecular gas surface density of a given GMC, with the conversion factor growing away from its minimum toward both low and high densities. This behavior is a consequence of two different effects taking place in the low- and high-density regimes. At high column densities the numerator in Equation (1) increases linearly, while the denominator (i.e., the CO intensity) is either constant or increases sub-linearly (as in the virialized cloud approximation for which $I(\mathrm{CO}) \propto \Delta v \propto \sqrt{N(\mathrm{H_2})}$). This effect is supported by spatially resolved observations of GMCs in the MW (Heiderman et al. 2010). Therefore X_{CO} increases toward high column densities. On the other hand, toward lower N(H2), the CO abundance drops due to CO dissociation as the dust extinction (which is proportional to the column density) decreases, giving rise to large "CO dark" envelopes and also implying an increase of X_{CO}. Both the location of the minimum, and the value of X_{CO} at the minimum are strong functions of the metallicity in the model.

When attempting to study these trends on kiloparsec scales within or across galaxies, we must take into account the fact that we measure averages for ensembles of molecular clouds with a distribution in their physical properties. In the Feldmann et al. (2012a) model, this average washes away the dependence on column density seen on small scales, and the authors predict almost no variation in X_{CO} as a function of H_2 surface density. It is important to point out that in this model the molecular gas temperature is fixed to 10 K in the calculation of I(CO), and the authors either impose a constant CO line width, or assume virialized clouds (i.e., $\Delta v \propto \sqrt{N(\mathrm{H_2})}$).

As discussed in the previous section, the models of Narayanan et al. (2012) and Feldmann et al. (2012a) predict similar behaviors for X_{CO} as a function of metallicity. On the other hand, the simulations conducted by Narayanan et al. (2012) do not assume a fixed temperature for the molecular component of the ISM, and instead include relevant heating and cooling calculations, which allow the authors to trace the molecular gas temperature. Furthermore, for molecular clouds which are larger than the spatial resolution of the simulation, they use the simulations themselves to follow the dynamical state of the molecular gas (i.e., the gas velocity dispersion sets the CO line width). For sub-resolution clouds they assume virialization.

The ability to follow the temperature and dynamical state of the gas allows Narayanan et al. (2012) to study the impact of turbulence and heating from both ongoing star formation, and large-scale gas dynamics, on the X_{CO} factor under high-density conditions like the ones present in starbursts, mergers, and the central regions of galaxies. While gas density itself should have little direct impact on X_{CO} when averaging over kiloparsec scales, the existence of a correlation like the SFL implies that higher molecular gas density is accompanied by stronger star formation activity. Star formation is associated with feedback from protostellar jets, stellar winds, and supernova (SN) explosions, as well as heating (both photoelectric and by cosmic rays produced in SNe), which rises both the temperature and turbulence of the gas. Furthermore, high-density regions are also commonly associated with dynamically violent environments, in which for example, merger-induced shocks and cloud–cloud collisions can induce higher levels of turbulence in the gas. Given the optically thick nature of the CO(1–0) transition, any turbulence-induced line broadening translates into a brighter I(CO) and a lower X_{CO}. Similarly, a higher gas temperature translates into a higher brightness temperature for the CO line. By construction, these effects are not recovered in the Feldmann et al. (2012a) simulations.

Comparing the observed dependence of X_{CO} with gas surface density, or with CO surface brightness, to theoretical numerical model predictions is challenging, and a series of caveats arise which must be kept in mind when interpreting this type of comparison. These caveats arise on one side from the limitations of the observations, where the large physical spatial resolution typically achieved in extragalactic studies (∼600 pc in NGC 628 for the HERACLES beam size) dilutes the actual surface brightness (or mass surface density) of GMCs in the beam, by some factor which depends on both the intrinsic surface brightness distribution of the clouds, and the covering fraction of clouds across the area over which the emission is being integrated. In denser regions, overlap of optically thick clouds can also affect the measured surface brightness. On the other hand, in numerical simulations, while physical numerical quantities are readily accessible, the definition of a "cloud," and the exact method used to measure its surface brightness or density can be non-trivial. This can be especially problematic when the resolution of the simulation is larger, or of the same order of magnitude as the typical sizes of clouds.

Narayanan et al. (2012) define X_{CO} as the ratio between the average column density, and the average CO intensity (luminosity divided by area) for each of their simulated galaxies, and provide a fitted formula to calculate X_{CO} from measurements of the metallicity ($Z' = Z/Z_{\odot}$) and the luminosity-weighted CO intensity of GMCs ($\langle I(\mathrm{CO})_{\mathrm{GMC}} \rangle$) in a galaxy:

$$X_{\mathrm{CO}} = \frac{\min[4,\ 6.75 \times \langle I(\mathrm{CO})_{\mathrm{GMC}} \rangle^{-0.32}] \times 10^{20}}{Z'^{0.65}}. \quad (4)$$

Unfortunately, $\langle I(\mathrm{CO})_{\mathrm{GMC}}\rangle$ is not recoverable by CO observations at kiloparsec scales, and also note that it is not the same quantity used in their definition of X_{CO}. Instead, of the luminosity-weighted average of the CO intensity of individual clouds, we measure the average CO intensity over large areas of the galactic disk of NGC 628, which is equivalent to the average intensity going in the definition of X_{CO} in the model.

Because of averaging over large areas, with a lower than unity cloud filling factor, our measured $I(\mathrm{CO})$ values should be significantly lower than the CO intensities one would measure for individual GMCs. In order to use the Narayanan et al. (2012) model to make meaningful predictions from our data, we adopt a "clumping factor" to scale our observed average CO intensities, in an attempt to recover the luminosity-weighted average intensity of individual GMC in the observed regions. A similar approach is adopted by Krumholz et al. (2009) to transform observed average H_2 surface densities into intrinsic GMC surface densities for input to their SFL model.

The choice of the clumping factor is somewhat arbitrary, but it only affects the absolute value of the predicted X_{CO} factors, and not any relative trends observed across the galaxy. We use a factor of 30 to scale up the observed $I(\mathrm{CO})$ values for input into Equation (10) in Narayanan et al. (2012). The justification for adopting this value is as follows. For an MW X_{CO} factor (which is consistent with the average factor we measure in NGC 628), the average CO intensity of NGC 628 inside a 7 kpc radius implies a mean value of Σ_{H2} which is nine times lower than the typical surface density of $\Sigma_{\mathrm{H2}} \simeq 100\,M_{\odot}\ \mathrm{pc}^{-2}$ measured for GMCs in the MW and the Local Group (Roman-Duval et al. 2010; Rosolowsky et al. 2003; Bolatto et al. 2008). On the other hand, comparison of Equations (6) and (10) in Narayanan et al. (2012) implies that in their model $\Sigma_{\mathrm{H2}} \propto \langle I(\mathrm{CO})_{\mathrm{GMC}}\rangle^{0.64}$. Therefore, a clumping factor of $30 \simeq 9^{1/0.64}$ would imply that the luminosity-weighted average GMC surface density in the inner 7 kpc of NGC 628 is similar to the typical MW and Local Group value.

The predicted X_{CO} values for different radial bins in NGC 628, computed using the measured metallicity and observed CO intensity (average between the HERACLES, BIMA, and CARMA measurements) corrected by this clumping factor, are shown as blue stars in Figure 5. Predictions for the Feldmann et al. (2012a) model would fall right on top of one of the two cyan solid lines in Figure 5, as in their parameterization X_{CO} is independent of Σ_{H2} and $I(\mathrm{CO})$. As stated in Section 5, the Narayanan et al. (2012) model is in better agreement with our data than the model of Feldmann et al. (2012a).

Figure 6 presents a comparison between the average X_{CO} values for each radial bin in NGC 628 (red stars) and the values predicted by the Narayanan et al. (2012) model (blue stars). Both are presented as a function of $I(\mathrm{CO})$ scaled by a clumpiness factor of 30, which, as stated above, should be roughly equivalent to the input $\langle I(\mathrm{CO})_{\mathrm{GMC}}\rangle$ for the model. By inspecting Figures 5 and 6 we can see that the model reproduces very well the observed trends in X_{CO} with both metallicity and CO surface brightness for the inner three radial bins in NGC 628. The slopes of both trends are consistent, and the absolute values agree to 1σ.

A caveat to the above approach is that adopting a single clumpiness parameter is equivalent to assuming a constant cloud filling factor over the observed area. A decrease in the cloud filling factor toward the outer disk is in fact likely, and could indeed explain both the flattening seen in X_{CO} for the $N = 1$ case when using the stacked Schruba et al. (2011) data in the outer disk of NGC 628, and the discrepancy observed between the data and the Narayanan et al. (2012) model for the outer radian bin. This latter discrepancy is reduced if one assumes $N = 1.5$ instead of $N = 1$ for the SFL.

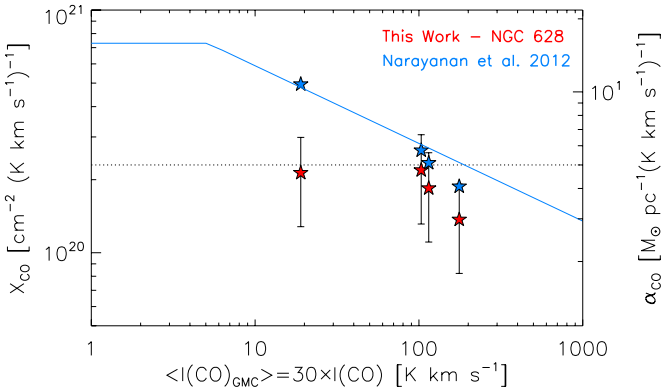

Figure 6. X_{CO} as a function of CO surface brightness for the four radial bins studied in NGC 628. CO intensities have been scaled by a clumpiness parameter of 30. Red stars show our measurements and blue stars show the predictions from the Narayanan et al. (2012) model using the metallicity and CO intensity of each bin. The solid blue line shows the predictions from the model at constant metallicity (the characteristic metallicity at 0.4 R_{25}). The horizontal dotted line shows the canonical MW value from Pineda et al. (2010).

(A color version of this figure is available in the online journal.)

At this point, it is important to remind the reader about the many scaling factors which affect the normalization of the X_{CO} values. These include the zero points in the flux calibration of the HERACLES CO and VENGA Hα maps, and the adopted Hα SFR calibration (we have scaled the other data sets to this reference), the adopted offsets used to match the metallicity scale of the different data sets and the models, and the adopted clumpiness parameter which is constrained only by demanding a typical GMC surface density of $\Sigma_{\mathrm{H2}} \simeq 100\,M_{\odot}\ \mathrm{pc}^{-2}$. Given the inherent systematic uncertainties associated with all these scaling factors, it is difficult to draw strong conclusions from the relative offset seen between the observed and predicted X_{CO} values. None of these scaling factors affect the relative trends seen across different radial bins in both the data and the model.

The main conclusion we can draw from the above comparison is the following. Our observations are in good agreement with the Narayanan et al. (2012) model. If X_{CO} follows the metallicity and CO brightness dependence proposed in this model, that is $X_{\mathrm{CO}} \propto \langle I(\mathrm{CO})_{\mathrm{GMC}}\rangle^{-0.32} \times Z'^{-0.65}$, then, the observed metallicity and CO surface brightness gradients imply that both quantities contribute to the formation of an X_{CO} gradient across the disk of NGC 628. As stated in Section 5, the measured metallicity gradient implies $Z' \propto 10^{-0.04R}$, and a linear fit to the CO surface brightness of the inner three radial bins ($R < 5$ kpc) implies $\langle I(\mathrm{CO})_{\mathrm{GMC}}\rangle \propto 10^{-0.07R}$. The model implies that $X_{\mathrm{CO}} \propto 10^{(0.32\times0.07+0.65\times0.04)R}$, or a gradient of $\Delta\log(X_{\mathrm{CO}}) = 0.05$ dex kpc^{-1}, in excellent agreement with the measured gradient of $\Delta\log(X_{\mathrm{CO}}) = 0.06 \pm 0.02$ dex kpc^{-1}. From the above calculation it can be seen that both the metallicity and the CO surface brightness (or equivalently the molecular gas surface density) contribute to the observed X_{CO} gradient. The Narayanan et al. (2012) prescription, in which X_{CO} is inversely proportional to the metallicity, and inversely proportional to the square root of the molecular gas surface density, is consistent with our data.

Our results indicate that across the disk of NGC 628, both the metallicity and the molecular gas surface density (through

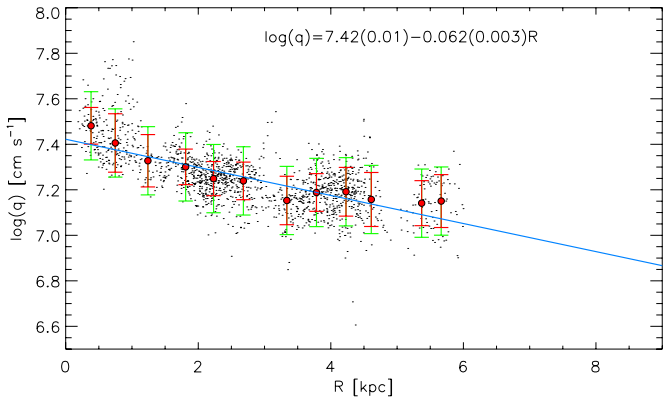

Figure 7. Ionization parameter as a function of radius in NGC 628. Black dots correspond to spaxels dominated by H II region emission in the VENGA data cube. Red circles show the median values in 0.5 kpc wide radial bins, and red and green error bars show the standard deviation in each bin and the systematic uncertainty in the calibration, respectively.

(A color version of this figure is available in the online journal.)

its incidence in the temperature and turbulence of the gas) are important factors setting the CO to H_2 conversion factor. Future analysis of a larger subset of the VENGA sample will allows us to know if this result is general enough to be applicable to most massive spiral galaxies in the local universe.

6.2. X_{CO} and the UV Radiation Field

In this section we use the ionization parameter, as measured from H II region emission line ratios in the VENGA data, as a proxy for the intensity of the local interstellar UV radiation field S_{UV} across the disk of NGC 628. The goal is to study the potential effect that the UV radiation field has at setting the value of X_{CO}.

The strength of the local UV radiation field has been proposed as an important factor setting the CO to H_2 conversion factor. Analyzing a sample of individual molecular complexes in the Large Magellanic Cloud and the Small Magellanic Cloud, Israel (1997) finds a linear correlation between the X_{CO} and the ratio of the far-IR surface brightness to H I column density ($\sigma_{FIR}/N(H\,I)$) which the author considers a proxy for the local UV radiation field per hydrogen atom (reprocessed after absorption and reemission by dust).

The effect of the UV radiation field on X_{CO} is also discussed by Feldmann et al. (2012a) in the context of their numerical simulations and their model of CO emission. The authors propose that for a single molecular cloud, the CO abundance decreases in the presence of a stronger UV radiation field U_{UV} (which they parameterize in units of the local interstellar UV radiation field, so $U_{UV} = S_{1000\,Å}/S_{MW}$, with $S_{MW} = 10^6$ photons cm^{-2} s^{-1} eV^{-1}). This dependence is stronger at low A_V (i.e., low $N(H_2)$, or low Z, or both), but an order of magnitude change in U_{UV} can still change the CO abundance by factors of a few at $A_V = 1$–3 mag. These extinction levels correspond to the outer envelopes CO emitting regions in GMCs, where CO(1–0) is starting to become optically thick. As the UV radiation field goes up, the CO abundance goes down, and X_{CO} increases for a single cloud (see their Figure 2).

When investigating this effect on galactic scales, Feldmann et al. (2012a) find that the strong dependence of X_{CO} with the UV radiation field present in their model for single GMCs at fixed $N(H_2)$ is completely suppressed in their simulated galaxies. This is due to the fact that in the simulations, physical parameters are measured over ensembles of molecular clouds with a distribution in their properties, and the abundance of clouds with low A_V, and therefore high X_{CO}, decreases strongly for higher values of the UV radiation field. In the Feldmann et al. (2012a) simulations, increasing U_{UV} suppresses the low-density tail of the N(H2) distribution function, dissociating diffuse molecular clouds with low densities ($\lesssim 10^{21}$ cm^{-2}) which have large X_{CO} values. Therefore, when averaging over kiloparsec scales, the radiation field has little impact in the average X_{CO} value, which is dominated by the surviving higher density regions with $N(H_2) \simeq 10^{22}$ cm^{-2}.

A competing effect, which might be important at setting the value of X_{CO}, is photoelectric heating working on large polycyclic aromatic hydrocarbon molecules and small dust grains in the outer envelopes of molecular clouds (Tielens 2005; Glover et al. 2010). The photoelectric heating rate is directly proportional to the intensity of the interstellar UV radiation field (Tielens 2005), therefore, the gas temperature and the CO transition brightness temperature can be increased in the presence of a stronger UV radiation field. By construction, this effect cannot be recovered by Feldmann et al. (2012a) as the authors impose a constant molecular gas temperature of 10 K in their simulations. This effect might be present in the Narayanan et al. (2012) simulations, which follow the main heating and cooling processes in the gas, and are able to trace changes in the gas temperature, though the authors do not attempt to separate it from dynamical effects on the brightness of the CO line. As mentioned above, part of the dependence of X_{CO} with molecular gas surface density might indeed be associated with this mechanism, as higher gas density translates into higher star formation activity and hence, a stronger interstellar UV radiation field.

In Figure 7 we present the radial distribution of the ionization parameter

$$q = \frac{S_{H^0}}{n}, \tag{5}$$

where S_{H^0} is the ionizing photon flux per unit area and n is the number density of hydrogen atoms. We have estimated q from the [O III] λ5007/[O II] λ3727 line ratio, as measured from the VENGA data cube of NGC 628, following the iterative procedures described in Kobulnicky & Kewley (2004). The measurements are limited to spaxels dominated by H II region emission (black dots) as in the case of the metallicity measurements described in Section 5.1. Red circles in Figure 7 show median values in at low densities ($\lesssim 10^{21}$ cm^{-2}) 0.5 kpc wide radial bins, and red and green error bars show the standard deviation in each bin and the systematic uncertainty in the calibration, respectively.

In NGC 628, the ionization parameter falls toward larger radii. A linear fit implies a gradient of $\Delta\log(q) = 0.061 \pm 0.003$ cm s^{-1} kpc^{-1}. A drop in the ionizing photon flux per hydrogen atom is consistent with the results of Aniano et al. (2012) who find a decreasing level of dust heating with radius due to a decrease in starlight intensity by modeling the *Spitzer*+*Herschel* spatially resolved dust SED of NGC 628. Considering the X_{CO} radial profile measured in Section 4, we find no evidence of an increase in X_{CO} in regions where the UV radiation field is enhanced, but we rather observe the opposite trend. The increase in X_{CO} for higher U_{UV} expected on clouds scales in the model of Feldmann et al. (2012a), and observed on molecular complexes scales by Israel (1997), is not seen in kiloparsec scales across the disk of NGC 628. This could be cause in part by the effects of averaging over large ensembles

of clouds, discussed in Feldmann et al. (2012a) and described above, but this could only suppress this dependence.

The fact that we observe the opposite behavior is consistent with the photoelectric heating effect described above. It is difficult to decouple the impact that the UV radiation field might have on the gas temperature and hence, on the value of X_{CO}, from surface density dependence discussed in Section 6.1. All we can conclude, is that the observed radial distribution in the ionization parameter, implies that thermal effects might be important at setting X_{CO}. Further study will be necessary to properly model these thermal effects, and decouple them from dynamical effects which also impact the radiative transfer of CO photons.

7. CONCLUSIONS

By inverting the SFL we obtain an independent estimate of the H_2 surface density across the disk of NGC 628 from the measured SFR surface density. Comparison to the observed CO intensity yields a measurement of the ^{12}CO(1–0) to H_2 conversion factor (X_{CO}). By studying the radial profile of X_{CO}, and its relation to other quantities like the metallicity, CO surface brightness, and the ionization parameter across the disk of the galaxy we reach the following conclusions.

1. The X_{CO} factor increases as a function of radius across the disk of NGC 628. A linear fit to the data in the inner 7 kpc of the galaxy implies a gradient of $\Delta\log(X_{CO}) = 0.06 \pm 0.02$ dex kpc^{-1} under the assumption of an $N = 1$ SFL slope. The radial profile is in agreement with measurements using an independent technique based on dust emission modeling and simultaneous fitting of the dust-to-gas ratio and the X_{CO} conversion (Sandstrom et al. 2012).
2. The observed X_{CO} radial profile is independent of the adopted SFR tracer (Hα versus FUV+24 μm), and the CO emission map used (single-dish versus interferometer, CO(1–0) versus CO(2–1)).
3. The observed X_{CO} radial profile is robust against changes in the adopted slope for the SFL ($N = 1$ versus 1.5). While assuming a steeper slope slightly steepens the observed profile, the effect is small compared to the changes seen in X_{CO} as a function of radius in NGC 628. The observed radial profile is robust, and it is not strongly affected by potential changes in the shape of the assumed SFL across the galaxy.
4. The observed metallicity gradient in NGC 628 implies that regions of lower metallicity show larger X_{CO} values. This is in agreement with integrated measurements across samples of galaxies in the local universe, and the predictions of theoretical models of CO emission in molecular gas.
5. Regions of lower CO surface brightness show higher X_{CO} values. This is in agreement with theoretical models which predict an enhanced escape probability of CO photons in higher density regions, due to an enhanced star formation activity which translates in a broadening of the CO line due to elevated gas temperatures and turbulence.
6. Informed by the theoretical model of Narayanan et al. (2012) we conclude that both the dependences with metallicity and H_2 surface density contribute in roughly similar amounts to the formation of the observed gradient in X_{CO}.
7. The ionization parameter shows a linear decreasing gradient as a function of radius, so regions where the intensity of the UV radiation field is higher show lower values of X_{CO}. This suggest that photoelectric heating might have an impact at setting the brightness temperature of the CO line, and therefore the value of the CO to H_2 conversion factor.
8. When comparing with theoretical models, our observations agree very well with the predictions of Narayanan et al. (2012). While our data also agree with the model of Feldmann et al. (2012a) in the slope of the X_{CO}–metallicity relation, and the lack of dependence of X_{CO} with the local ionizing field on kiloparsec scales, this model predicts X_{CO} values which are typically a factor of $\sim$4 higher than the observed ones.
9. Given the observed X_{CO} radial profile in NGC 628, we conclude that using a single MW X_{CO} factor to estimate the total H_2 mass would imply an overestimation of 20% in this quantity. While this is a relatively small effect, our results imply that much larger systematic deviations can occur when using a canonical value in specific regions within galaxies, or when the local conditions of the ISM in the regions of interest differ significantly from the canonical values.

A series of assumptions have been made in order to reach these conclusions, and it is important to keep these in mind while interpreting our results. The uncertainty in the flux calibration and sensitivity to emission on different spatial scales in the three CO data sets used, the use of a constant non-radially dependent CO(2–1) to CO(1–0) ratio to scale the HERACLES data, the uncertainty in extinction correction (in the case of Hα) and the SFR calibrations used for Hα and FUV plus 24 μm, and the assumption that a single molecular SFL holds across the disk of the galaxy, all add up to make the systematic uncertainty in the absolute value of X_{CO} values large. An important assumption made is that all these uncertain scaling factors do not have a strong radial dependence, therefore allowing for the relative radial trend in X_{CO} to be measured. This assumption is supported by the fact that the six combinations of data sets used in this study, as well as independent measurements from dust SED modeling (Sandstrom et al. 2012), show similar trend of an increasing X_{CO} with radius.

In the future, we expect to extend this study to a larger sample of galaxies in the VENGA survey, in order to confirm if the observed trends are a common feature among massive spirals in the local universe. In the near future, ALMA will allow us to study molecular complexes in nearby galaxies like NGC 628, in the same level of detail that we can currently achieve in the MW. In the context of this study, the commissioning of the MUSE IFU in the Very Large Telescope will provide an instrument with excellent spatial resolution over a large field of view, which could be the perfect complement for ALMA observations of nearby galaxies.

The VENGA Collaboration acknowledges the generous support from the Norman Hackerman Advanced Research Program (NHARP) ARP-03658-0234-2009, G.A.B. acknowledges the support of Sigma Xi, The Scientific Research Society, Grant-in-Aid of Research. N.J.E. acknowledges the support of NSF grant AST 1109116. A.D.B. acknowledges partial support from grants NSF AST-0838178, NSF AST-0955836, as well as a Cottrell Scholar award from the Research Corporation for Science Advancement. N.D. acknowledges support from PAPIIT grant IA-100212. We also acknowledge Desika Narayanan for providing the curves presented in Figure 5, and for useful advice regarding the application of his model, and Karin Sandstrom useful discussions and for providing her data for comparison. Support for CARMA construction was derived from the

Gordon and Betty Moore Foundation, the Eileen and Kenneth Norris Foundation, the Caltech Associates, the states of California, Illinois, and Maryland, and the NSF. Funding for ongoing CARMA development and operations are supported by NSF and CARMA partner universities. The construction of the Mitchell Spectrograph (formerly VIRUS-P) was possible thanks to the generous support of the Cynthia & George Mitchell Foundation. This research has made use of NASA's Astrophysics Data System, and of the NASA/IPAC Extragalactic Database (NED) which is operated by the Jet Propulsion Laboratory, California Institute of Technology, under contract with the National Aeronautics and Space Administration.

REFERENCES

Abdo, A. A., Ackermann, M., Ajello, M., et al. 2010, ApJ, 710, 133
Adler, D. S., Lo, K. Y., Wright, M. C. H., et al. 1992, ApJ, 392, 497
Aniano, G., Draine, B. T., Calzetti, D., et al. 2012, ApJ, 756, 138
Arimoto, N., Sofue, Y., & Tsujimoto, T. 1996, PASJ, 48, 275
Bigiel, F., Leroy, A., Walter, F., et al. 2008, AJ, 136, 2846
Blanc, G. A., Gebhardt, K., Heiderman, A., et al. 2010, in ASP Conf. Ser. 432, New Horizons in Astronomy: Frank N. Bash Symposium 2009, ed. L. M. Stanford, J. D. Green, L. Hai, & Y. Mao (San Francisco, CA: ASP), 180
Blanc, G. A., Heiderman, A., Gebhardt, K., Evans, N. J., II, & Adams, J. 2009, ApJ, 704, 842
Blitz, L., Fukui, Y., Kawamura, A., et al. 2007, in Protostars and Planets V, ed. B. Reipurth, D. Jewitt, & K. Keil (Tucson, AZ: Univ. Arizona Press), 81
Bolatto, A. D., Jackson, J. M., & Ingalls, J. G. 1999, ApJ, 513, 275
Bolatto, A. D., Leroy, A. K., Rosolowsky, E., Walter, F., & Blitz, L. 2008, ApJ, 686, 948
Bryant, P. M., & Scoville, N. Z. 1999, AJ, 117, 2632
Calzetti, D., Kennicutt, R. C., Engelbracht, C. W., et al. 2007, ApJ, 666, 870
Calzetti, D., Liu, G., & Koda, J. 2012, ApJ, 752, 98
Chabrier, G. 2003, ApJL, 586, L133
Chomiuk, L., & Povich, M. S. 2011, AJ, 142, 197
Daddi, E., Elbaz, D., Walter, F., et al. 2010, ApJL, 714, L118
Dale, D. A., Cohen, S. A., Johnson, L. C., et al. 2009, ApJ, 703, 517
Dickman, R. L., Snell, R. L., & Schloerb, F. P. 1986, ApJ, 309, 326
Digel, S. W., Grenier, I. A., Heithausen, A., Hunter, S. D., & Thaddeus, P. 1996, ApJ, 463, 609
Downes, D., & Solomon, P. M. 1998, ApJ, 507, 615
Feldmann, R., Gnedin, N. Y., & Kravtsov, A. V. 2012a, ApJ, 747, 124
Feldmann, R., Gnedin, N. Y., & Kravtsov, A. V. 2012b, ApJ, 758, 127
Fukui, Y., & Kawamura, A. 2010, ARA&A, 48, 547
García-Burillo, S., Usero, A., Alonso-Herrero, A., et al. 2012, A&A, 539, A8
Genzel, R., Tacconi, L. J., Combes, F., et al. 2012, ApJ, 746, 69
Genzel, R., Tacconi, L. J., Gracia-Carpio, J., et al. 2010, MNRAS, 407, 2091
Gil de Paz, A., Boissier, S., Madore, B. F., et al. 2007, ApJS, 173, 185
Glover, S. C. O., Federrath, C., Mac Low, M.-M., & Klessen, R. S. 2010, MNRAS, 404, 2
Gutiérrez, L., Beckman, J. E., & Buenrostro, V. 2011, AJ, 141, 113
Hao, C.-N., Kennicutt, R. C., Johnson, B. D., et al. 2011, ApJ, 741, 124
Heiderman, A., Evans, N. J., II, Allen, L. E., Huard, T., & Heyer, M. 2010, ApJ, 723, 1019
Helfer, T. T., Thornley, M. D., Regan, M. W., et al. 2003, ApJS, 145, 259
Herrmann, K. A., Ciardullo, R., Feldmeier, J. J., & Vinciguerra, M. 2008, ApJ, 683, 630
Heyer, M. H., Carpenter, J. M., & Snell, R. L. 2001, ApJ, 551, 852
Israel, F. P. 1997, A&A, 328, 471
Kennicutt, R. C., Calzetti, D., Aniano, G., et al. 2011, PASP, 123, 1347
Kennicutt, R. C., Jr. 1998, ApJ, 498, 541
Kennicutt, R. C., Jr., Armus, L., Bendo, G., et al. 2003, PASP, 115, 928
Kennicutt, R. C., Jr., Calzetti, D., Walter, F., et al. 2007, ApJ, 671, 333
Kennicutt, R. C., Jr., & Evans, N. J., II 2012, ARA&A, 50, 531
Kennicutt, R. C., Jr., Hao, C.-N., Calzetti, D., et al. 2009, ApJ, 703, 1672
Kewley, L. J., & Dopita, M. A. 2002, ApJS, 142, 35
Kewley, L. J., & Ellison, S. L. 2008, ApJ, 681, 1183
Kobulnicky, H. A., & Kewley, L. J. 2004, ApJ, 617, 240
Kroupa, P., & Weidner, C. 2003, ApJ, 598, 1076
Krumholz, M. R., Leroy, A. K., & McKee, C. F. 2011, ApJ, 731, 25
Krumholz, M. R., McKee, C. F., & Tumlinson, J. 2009, ApJ, 699, 850
Kuno, N., Sato, N., Nakanishi, H., et al. 2007, PASJ, 59, 117
Leroy, A. K., Bigiel, F., de Blok, W. J. G., et al. 2012, AJ, 144, 3
Leroy, A. K., Bolatto, A., Gordon, K., et al. 2011, ApJ, 737, 12
Leroy, A. K., Walter, F., Bigiel, F., et al. 2009, AJ, 137, 4670
Leroy, A. K., Walter, F., Brinks, E., et al. 2008, AJ, 136, 2782
Liu, G., Koda, J., Calzetti, D., Fukuhara, M., & Momose, R. 2011, ApJ, 735, 63
Madore, B. F. 2010, ApJL, 716, L131
Maloney, P., & Black, J. H. 1988, ApJ, 325, 389
Mauersberger, R., Henkel, C., Whiteoak, J. B., Chin, Y.-N., & Tieftrunk, A. R. 1996, A&A, 309, 705
McQuinn, K. B. W., Skillman, E. D., Dalcanton, J. J., et al. 2012, ApJ, 751, 127
Meier, D. S., & Turner, J. L. 2004, AJ, 127, 2069
Meier, D. S., Turner, J. L., & Hurt, R. L. 2008, ApJ, 675, 281
Meier, D. S., Turner, J. L., Beck, S. C., et al. 2010, AJ, 140, 1294
Moustakas, J., Kennicutt, R. C., Jr., Tremonti, C. A., et al. 2010, ApJS, 190, 233
Murphy, E. J., Condon, J. J., Schinnerer, E., et al. 2011, ApJ, 737, 67
Narayanan, D., Krumholz, M. R., Ostriker, E. C., & Hernquist, L. 2012, MNRAS, 421, 3127
Oka, T., Hasegawa, T., Hayashi, M., Handa, T., & Sakamoto, S. 1998, ApJ, 493, 730
Onodera, S., Kuno, N., Tosaki, T., et al. 2010, ApJL, 722, L127
Pilyugin, L. S., & Thuan, T. X. 2005, ApJ, 631, 231
Pineda, J. L., Goldsmith, P. F., Chapman, N., et al. 2010, ApJ, 721, 686
Rahman, N., Bolatto, A. D., Xue, R., et al. 2012, ApJ, 745, 183
Regan, M. W. 2000, ApJ, 541, 142
Roman-Duval, J., Jackson, J. M., Heyer, M., Rathborne, J., & Simon, R. 2010, ApJ, 723, 492
Rosales-Ortega, F. F., Díaz, A. I., Kennicutt, R. C., & Sánchez, S. F. 2011, MNRAS, 415, 2439
Rosolowsky, E., Engargiola, G., Plambeck, R., & Blitz, L. 2003, ApJ, 599, 258
Salpeter, E. E. 1955, ApJ, 121, 161
Sandstrom, K. M., Leroy, A. K., Walter, F., et al. 2012, ApJ, submitted (arXiv:1212.1208)
Schmidt, M. 1959, ApJ, 129, 243
Schruba, A., Leroy, A. K., Walter, F., Sandstrom, K., & Rosolowsky, E. 2010, ApJ, 722, 1699
Schruba, A., Leroy, A. K., Walter, F., et al. 2011, AJ, 142, 37
Schruba, A., Leroy, A. K., Walter, F., et al. 2012, AJ, 143, 138
Shetty, R., Glover, S. C., Dullemond, C. P., et al. 2011, MNRAS, 415, 3253
Shier, L. M., Rieke, M. J., & Rieke, G. H. 1994, ApJL, 433, L9
Sodroski, T. J., Odegard, N., Dwek, E., et al. 1995, ApJ, 452, 262
Solomon, P. M., Downes, D., Radford, S. J. E., & Barrett, J. W. 1997, ApJ, 478, 144
Solomon, P. M., & Vanden Bout, P. A. 2005, ARA&A, 43, 677
Strong, A. W., Moskalenko, I. V., Reimer, O., Digel, S., & Diehl, R. 2004, A&A, 422, L47
Tacconi, L. J., Genzel, R., Smail, I., et al. 2008, ApJ, 680, 246
Tielens, A. G. G. M. 2005, The Physics and Chemistry of the Interstellar Medium (Cambridge: Cambridge Univ. Press)
Verley, S., Corbelli, E., Giovanardi, C., & Hunt, L. K. 2010, A&A, 510, A64
Vila-Vilaró, B. 2008, PASJ, 60, 1231
Wall, W. F., Jaffe, D. T., Bash, F. N., et al. 1993, ApJ, 414, 98
Wild, W., Harris, A. I., Eckart, A., et al. 1992, A&A, 265, 447
Wilson, C. D. 1995, ApJL, 448, L97